The Astrophysical Journal, 948:137 (27pp), 2023 May 10 https://doi.org/10.3847/1538-4357/acc2b9

Volumetric Rates of Luminous Red Novae and Intermediate-luminosity Red Transients with the Zwicky Transient Facility

Viraj R. Karambelkar[1], Mansi M. Kasliwal[1], Nadejda Blagorodnova[2], Jesper Sollerman[3], Robert Aloisi[4], Shreya G. Anand[1], Igor Andreoni[5,6,7], Thomas G. Brink[8], Rachel Bruch[9], David Cook[10], Kaustav Kashyap Das[1], Kishalay De[11], Andrew Drake[1], Alexei V. Filippenko[8], Christoffer Fremling[1,12], George Helou[10], Anna Ho[13], Jacob Jencson[14], David Jones[15,16,17], Russ R. Laher[10], Frank J. Masci[10], Kishore C. Patra[18], Josiah Purdum[12], Alexander Reedy[1], Tawny Sit[19], Yashvi Sharma[1], Anastasios Tzanidakis[20], Stéfan J. van der Walt[21], Yuhan Yao[1], and Chaoran Zhang[22]

[1] Cahill Center for Astrophysics, California Institute of Technology, Pasadena, CA 91125, USA; viraj@astro.caltech.edu
[2] Department of Astrophysics/IMAPP, Radboud University, Nijmegen, The Netherlands
[3] The Oskar Klein Centre, Department of Astronomy, Stockholm University, AlbaNova, SE-10691 Stockholm, Sweden
[4] Department of Astronomy, University of Wisconsin-Madison, 475 North Charter Street, Madison, WI 53706, USA
[5] Joint Space-Science Institute, University of Maryland, College Park, MD 20742, USA
[6] Department of Astronomy, University of Maryland, College Park, MD 20742, USA
[7] Astrophysics Science Division, NASA Goddard Space Flight Center, Mail Code 661, Greenbelt, MD 20771, USA
[8] Department of Astronomy, University of California, Berkeley, CA 94720-3411, USA
[9] Department of Particle Physics and Astrophysics, Weizmann Institute of Science, 234 Herzl St, 76100 Rehovot, Israel
[10] IPAC, California Institute of Technology, 1200 E. California Blvd, Pasadena, CA 91125, USA
[11] MIT-Kavli Institute for Astrophysics and Space Research, 77 Massachusetts Ave., Cambridge, MA 02139, USA
[12] Caltech Optical Observatories, California Institute of Technology, Pasadena, CA 91125, USA
[13] Department of Astronomy, Cornell University, Ithaca, NY 14853, USA
[14] Department of Physics and Astronomy, Johns Hopkins University, 3400 North Charles Street, Baltimore, MD 21218, USA
[15] Instituto de Astrofísica de Canarias, E-38205 La Laguna, Tenerife, Spain
[16] Departamento de Astrofísica, Universidad de La Laguna, E-38206 La Laguna, Tenerife, Spain
[17] Nordic Optical Telescope, Rambla José Ana Fernández Pérez 7, E-38711, Breña Baja, Spain
[18] Nagaraj-Noll-Otellini Graduate Fellow, Department of Astronomy, University of California, Berkeley, CA 94720-3411, USA
[19] Department of Astronomy, The Ohio State University, 140 West 18th Avenue, Columbus, OH 43210, USA
[20] Department of Astronomy, University of Washington, Seattle, WA 98195, USA
[21] Berkeley Institute for Data Science, University of California, Berkeley, USA
[22] Center for Gravitation, Cosmology, and Astrophysics, Department of Physics, University of Wisconsin, Milwaukee, WI 53201, USA
Received 2022 November 8; revised 2023 March 1; accepted 2023 March 6; published 2023 May 17

Abstract

Luminous red novae (LRNe) are transients characterized by low luminosities and expansion velocities, and they are associated with mergers or common-envelope ejections in stellar binaries. Intermediate-luminosity red transients (ILRTs) are an observationally similar class with unknown origins, but they are generally believed to be either electron-capture supernovae in super-asymptotic giant branch stars or outbursts in dusty luminous blue variables (LBVs). In this paper, we present a systematic sample of eight LRNe and eight ILRTs detected as part of the Census of the Local Universe (CLU) experiment on the Zwicky Transient Facility (ZTF). The CLU experiment spectroscopically classifies ZTF transients associated with nearby (<150 Mpc) galaxies, achieving 80% completeness for $m_r < 20$ mag. Using the ZTF-CLU sample, we derive the first systematic LRNe volumetric rate of $7.8^{+6.5}_{-3.7} \times 10^{-5}$ Mpc^{-3} yr^{-1} in the luminosity range $-16 \leqslant M_r \leqslant -11$ mag. We find that, in this luminosity range, the LRN rate scales as $dN/dL \propto L^{-2.5\pm0.3}$—significantly steeper than the previously derived scaling of $L^{-1.4\pm0.3}$ for lower-luminosity LRNe ($M_V \geqslant -10$ mag). The steeper power law for LRNe at high luminosities is consistent with the massive merger rates predicted by binary population synthesis models. We find that the rates of the brightest LRNe ($M_r \leqslant -13$ mag) are consistent with a significant fraction of them being progenitors of double compact objects that merge within a Hubble time. For ILRTs, we derive a volumetric rate of $2.6^{+1.8}_{-1.4} \times 10^{-6}$ Mpc^{-3} yr^{-1} for $M_r \leqslant -13.5$ mag, which scales as $dN/dL \propto L^{-2.5\pm0.5}$. This rate is ∼1%–5% of the local core-collapse supernova rate and is consistent with theoretical ECSN rate estimates.

Unified Astronomy Thesaurus concepts: Binary stars (154); Common-envelope evolution (2154); Time-domain astronomy (2109); Transient sources (1851); Core-collapse supernovae (304); Luminous blue variable stars (944)

1. Introduction

The advent of time-domain surveys in the last few decades has led to the discovery of "gap transients"—a new class of explosions that have $-16 \leqslant M_V \leqslant -10$ mag and occupy the luminosity gap between novae and supernovae (SNe; Kasliwal et al. 2011; Pastorello & Fraser 2019). This class includes a diverse variety of transients such as faint core-collapse SNe (Yang et al. 2021), .Ia-like SNe (Bildsten et al. 2007), low-luminosity Iax SNe (Karambelkar et al. 2021), luminous red novae (LRNe; Kulkarni et al. 2007), intermediate-luminosity red transients (ILRTs; Thompson et al. 2009), and outbursts in luminous blue variable (LBV) stars (Smith et al. 2011). Among

gap transients, there is a subclass of hydrogen-rich explosions characterized by low expansion velocities and interaction with surrounding circumstellar material (CSM). This subclass comprises LRNe, ILRTs, and LBV outbursts.

LRNe are transients associated with the final stages of common-envelope evolution (CEE) in a stellar binary system (Tylenda 2005; Ivanova et al. 2013a; Pastorello et al. 2019a). The loss of angular momentum in a binary can initiate CEE that terminates with the inspiral of the binary on dynamical timescales. This can either lead to the merger of the two stars or the ejection of the CE and formation of a stable binary in a tighter orbit. Both cases are accompanied by energetic outbursts that are powered primarily by shocks or recombination in the ejected material (Ivanova et al. 2013a; MacLeod et al. 2017; Pejcha et al. 2017; Soker 2020; Soker & Kaplan 2021; Matsumoto & Metzger 2022). The association of LRNe with CE-related outbursts was supported by the discovery of V 1309Sco, a Galactic LRN with archival photometric data showing a binary with a rapidly decaying orbital period in the years leading to the transient (Tylenda et al. 2011). LRNe thus present an opportunity to probe the poorly understood physics of CEE; see Ivanova et al. (2013b). This is of particular importance because CEE is a crucial phase in the formation of double compact objects (DCOs; Vigna-Gómez et al. 2020) that merge to radiate gravitational waves, which are being detected regularly by LIGO (The LIGO Scientific Collaboration et al. 2021a).

LRNe generally have low expansion velocities (<1000 km s^{-1}), a wide range of luminosities ($-3 > M_V > -16$ mag), and long-lasting (∼100 days) multipeaked light curves that redden rapidly due to dust formation (Kamiński & Tylenda 2011; Kamiński et al. 2015). Prior to 2021, only four Galactic and 11 extragalactic LRNe were known (Kochanek et al. 2014; Blagorodnova et al. 2021, and references therein). The extragalactic LRNe have $-9 > M_{\rm peak} > -15$ mag, while the Galactic LRNe in general have much lower luminosities. Progenitor primary stars have been identified for seven LRNe so far and have revealed interesting correlations between the masses and peak luminosities (Pastorello et al. 2019a; Blagorodnova et al. 2021). Despite these advances, the volumetric rates of LRNe are largely unconstrained. The best estimate of the rate comes from Kochanek et al. (2014), who used three Galactic LRNe that had $-4 > M_V > -10$ mag discovered over the last 30 yr to determine their rate in the Milky Way. They find that very low-luminosity events ($M_{r/V,\rm peak} \approx -3$ mag) are fairly common (∼0.5 yr^{-1}), but the rate drops $\propto L^{-1.4}$ with increasing luminosity. The rate of the more-luminous, extragalactic LRNe has not been measured yet, and extrapolations based on the Galactic rate disagree by orders of magnitude with the expectations from population synthesis (Howitt et al. 2020). An accurate measurement of the rate and luminosity function of LRNe is needed in order to probe several CEE parameters (see Howitt et al. 2020 for examples).

ILRTs are an observationally related class of transients that are also characterized by low expansion velocities and reddening photometric evolution, but have single-peaked light curves and a narrower luminosity range ($-11 > M_V > -15$ mag) compared to LRNe (Cai et al. 2021). The origin of ILRTs still remains a mystery. They have been proposed to be electron-capture SNe (ECSNe) in super-asymptotic giant branch (AGB) stars (Botticella et al. 2009; Cai et al. 2021).[23] Both explanations are supported by the peculiar progenitors of ILRTs. The ILRTs SN 2008S, NGC 300 OT, and AT 2019abn have been associated with extremely dusty, infrared (IR)-bright progenitors (Prieto et al. 2008; Botticella et al. 2009; Jencson et al. 2019) consistent with super-AGB stars, while the proposed ILRT AT 2019krl was associated with a blue supergiant or LBV progenitor (Andrews et al. 2021). About a dozen ILRTs have been studied extensively in the last decade (see Cai et al. 2021 and references therein). Similarly to the case with LRNe, the volumetric rate has not been reliably measured. Based on two ILRTs (SN 2008S and NGC 300 OT), Thompson et al. (2009) estimate the ILRT rate to be ∼20% of the core-collapse SN (CCSN) rate. Cai et al. (2021) use a sample of five ILRTs reported by different surveys over the last decade and estimate a lower limit of ∼8% of the CCSN rate.

Reliable LRN and ILRT rate measurements have been hindered by their heterogeneous sample. The existing rate estimates have used transients reported by different surveys and have not accounted for effects of survey completeness or selection biases (Kochanek et al. 2014; Cai et al. 2021). A systematic sample of LRNe and ILRTs, preferably from a single survey, is required to accurately constrain their rate. Such studies are now possible with experiments like the Census of the Local Universe (CLU; De et al. 2020) on the Zwicky Transient Facility (ZTF; Bellm et al. 2019; Graham et al. 2019; Dekany et al. 2020). ZTF is an optical time-domain survey with a 47 sq. deg field of view that surveys the entire accessible northern sky at a cadence of ∼2–3 days in the g and r bands down to a depth of 20.5 mag. The CLU experiment aims to build a spectroscopically complete sample of transients detected by ZTF that are associated with galaxies in the CLU galaxy catalog (Cook et al. 2019) to a depth of $m_r \approx 20$ mag. The CLU experiment is ideal for detecting low-luminosity ($M_r \geq -16$ mag) transients like LRNe and ILRTs out to large distances (∼100 Mpc), consequently building a large sample of such rare transients.

In this paper, we present a systematic sample of LRNe and ILRTs detected by the ZTF CLU experiment from 2018 June 1 to 2022 February 20.[24] We utilize this sample and the actual observation history of ZTF to derive the rates of LRNe and ILRTs. In Section 2.1, we describe the selection criteria used to construct our LRN and ILRT samples. Section 2.1 also discusses the photometric and spectroscopic properties of LRNe and ILRTs identified in the CLU experiment. Our methods for deriving the luminosity function and volumetric rates of LRNe and ILRTs are described in Section 3. Section 4 compares our results to previous measurements and theoretical predictions, and discusses the implications for progenitors of LRNe and ILRTs. We conclude with a summary of our results in Section 5.

2. Sample Selection

2.1. Candidate Filtering

We focus our search on transients discovered as part of the ZTF CLU experiment (De et al. 2020). Briefly, CLU aims to build a spectroscopically complete sample of transients associated with galaxies in the local universe (<200 Mpc). The CLU experiment uses alerts generated from all three (public, collaboration, and Caltech) components of the ZTF

[23] ILRTs are also proposed to be failed supernovae in massive stars (Tsuna et al. 2020), but this model does not have strong evidence supporting it yet.

[24] UTC dates are used throughout this paper.

survey (see De et al. 2020 for details). CLU uses the platform `skyportal` to save and coordinate follow-up observations of sources (van der Walt et al. 2019). During ZTF Phase I (2018 June 1–2020 October 30), the experiment was limited to all transients that (1) were within 100″ of known galaxies in the CLU galaxy catalog (Cook et al. 2019), (2) had more than two detections in ZTF-g or r filters, and (3) were brighter than $m_r = 20$ mag. Starting 2020 October 30 (ZTF Phase II), the filtering criteria were updated to select transients that were (1) within 30 kpc of CLU galaxies closer than 140 Mpc, (2) brighter than $m_r = 20.5$ mag, and (3) less luminous than $M_r = -17$ mag. A total of 3442 transients have been saved by the CLU experiment since the start of the ZTF survey. The experiment achieved a spectroscopic completeness of 88.5% in ZTF Phase I and 79% in ZTF Phase II for sources brighter than 20 mag.

Candidate LRNe and ILRTs were selected from their real-time ZTF alert photometry using the following selection criteria:

1. the transient must pass the CLU selection criteria,
2. the transient must be less luminous than $M_r = -16$ mag, and
3. the transient must have two ZTF alerts (i.e., two $>5\sigma$ detections) brighter than 20 mag in either g or r.

The sample presented in this paper is restricted to events saved before 2022 February 20.

Five hundred and twenty-three transients satisfied the selection criteria listed above. One hundred and nine of these were found to lie on top of faint underlying galaxies that are not present in the CLU catalog. These transients were excluded because they are likely SNe in distant host galaxies. Fifty-five additional candidates were excluded because they were flagged as image-processing artifacts on visual inspection of the difference images. Seventy-three candidates were eliminated because they showed small, long-term (>1 yr) variations in brightness without significant color changes and were coincident with stars in the Milky Way or nearby galaxies (M31 or M33).

To further filter our candidates, we used follow-up spectroscopic observations (either from our own follow-up campaigns or on TNS). In addition to the CLU experiment, some of our spectra were collected as part of the ZTF Bright Transient Survey (BTS; Fremling et al. 2020; Perley et al. 2020). The BTS classifications are already public, while all CLU classifications will be presented in separate papers focusing on different subsamples (e.g., De et al. 2020; A. Tzanidakis et al. 2023, in preparation; Sit et al., submitted). Of the CLU transients that pass our criteria, seven sources were spectroscopically classified [based on the presence or absence of broad ($v \geqslant 5000$ km s^{-1}) H emission lines, and other characteristics] as active galactic nuclei (AGNs), 65 as hydrogen-poor SNe (Ia, Iax, Ca-rich, Ib, and Ic SNe), 11 as classical novae, and 128 as Type II SNe. Two additional candidates were studied in detail (Reguitti et al. 2021; Yang et al. 2021) as low-luminosity Type II SNe showing low-velocity H lines. We were then left with 73 sources that did not match any of the above categories.

We ran forced point-spread function (PSF) photometry at the location of these 73 sources on all ZTF difference images (Masci et al. 2019). This provides more accurate photometry than the real-time ZTF alerts, and it also enables the recovery of subthreshold ($>3\sigma$) detections. From this set, 14 candidates were ruled out because their forced photometry revealed them to have absolute magnitudes brighter than −16. Eighteen additional sources were eliminated because their forced-photometry light curves revealed slow, small-amplitude, long-term (>500 days) variations. These slowly varying sources are likely foreground variable stars, but some could also be long-duration giant outbursts in LBV stars such as η Car or UGC 2773-OT (Humphreys et al. 1999; Smith et al. 2016). One additional source at redshift $z = 0.002$ showed fast, erratic variations in ZTF data. Finally, five sources had $M_r \geqslant -10$ mag and rapidly fading light curves (<10 days), suggesting that they are classical novae. Of the remaining sources, one showed a declining light curve with $g - r < 0$ mag, similar to late-time SN light curves but unlike LRNe or ILRTs. The remaining 34 sources are promising LRN and ILRT candidates, and these are listed in Table 1.

2.2. Classification

The list of 34 transients in Table 1 consists of LRNe, ILRTs, LBV outbursts, and possibly some SNe observed at late phases. Here, we discuss the classifications of these transients using their ZTF light curves, spectroscopic data, and archival photometry.

LRNe typically exhibit multipeaked light curves (Pejcha et al. 2017; Matsumoto & Metzger 2022), which allow them to be photometrically differentiated from ILRTs (Cai et al. 2021). Table 1 indicates the transients that show multiple peaks in their ZTF light curves.

Searching for previous outbursts in archival data can help distinguish LBV eruptions from LRNe/ILRTs, as LBV outbursts can be recurring. While LRNe are also known to show precursor emission in the years leading up to the merger, the precursors usually have much lower luminosities than the actual merger. The detection of historic outbursts comparable in brightness to the latest outburst is thus suggestive of an LBV eruption. We checked for historical activity at the locations of these sources using data from the ATLAS (depth ∼19.5 mag, dating back to ∼2014; see Tonry et al. 2018; Smith et al. 2020) and PTF (depth ∼21.5 mag, dating back to ∼2009; see Law et al. 2009; Rau et al. 2009) surveys. All 34 sources have ATLAS data, while 15 have PTF data. Table 1 indicates which transients were detected in the archival ATLAS or PTF data. The full forced-photometry light curves will be available online (see Section 7).

Spectroscopic data is available for 19 of the 34 transients. The low spectroscopic completeness of this sample compared to the full CLU experiment is discussed in Section 3.3. Eleven of these sources only have medium-resolution optical spectra, while the remaining eight also have medium-resolution near-infrared (NIR) spectra. The optical spectra were taken with the Low-Resolution Imaging Spectrograph (LRIS; resolution $R \approx 750$; Oke et al. 1995) on the Keck I 10 m telescope, the Double Beam Spectrograph (DBSP; $R \approx 1000$; Oke & Gunn 1982) on the 200 inch Hale telescope (P200) on Mount Palomar, the Alhambra Faint Object Spectrograph and Camera (ALFOSC; $R \approx 360$) on the 2.56 m Nordic Optical Telescope (NOT), the Kast Double Spectrograph on the Shane 3 m telescope at Lick Observatory ($R \approx 1000$), and the Spectrograph for Rapid Acquisition of Transients (SPRAT; $R \approx 350$) on the Liverpool Telescope. For ZTF 21acpkzcc, we obtained a high-resolution ($R \approx 15{,}000$) spectrum with the South African Large Telescope High Resolution

Table 1
Properties of the 34 ZTF Transients of Interest

ZTF Name	AT Name	M_{abs} at Peak	Multipeak/ Plateau	Archival (PTF/ATLAS)	Gal type[b]	Hα-FWHM[c] (km s^{-1})	[Ca II]	Mol. Feats.	Classification
ZTF18acbwfza[a]	18hso	-13.82 ± 0.15	mp	−/no	SB(r)a pec	500	em?	yes[d]	LRN-gold
ZTF19adakuot	19zhd	-9.60 ± 0.15	pl	no/yes	SA(s)b			yes[c]	LRN-gold
ZTF20aawdwch[a]	20hat	-11.43 ± 0.15	pl	no/no	SAB(rs)cd	130	no	yes	LRN-gold
ZTF21aancgbm[a]	21biy	-13.86 ± 0.15	mp	yes/no	SB(s)d.	500	em?	yes	LRN-gold
ZTF21aagppzg[a]	21blu	-13.50 ± 0.15	mp	no/no	star-forming	500	no	yes	LRN-gold
ZTF21acpkzcc[a]	21aess	-15.12 ± 0.15	mp	−/no	SB(s)m?	500	no	⋯	LRN-gold
ZTF18abwxrhi[a]	18gzz	-14.50 ± 0.16	mp	no/no	(R')SB(rs)ab	300	no	no	LRN-silver
ZTF21aaekeqd[a]	21afy	-13.95 ± 0.16	pl	−/no	star-forming	700	no	no	LRN-silver
ZTF18aajgqmr	20ifb	-15.36 ± 0.17	mp	−/no	star-forming				LRN-bronze
ZTF20abjgdec	20afdb	-14.37 ± 0.16	mp	−/no	star-forming				LRN-bronze
ZTF21aabfwwl	21iy	-15.72 ± 0.16	mp	−/no	star-forming				LRN-bronze
ZTF18acdyopn	18hcj	-14.33 ± 0.19	no	−/no	SAdm.	300	em	no	ILRT-gold
ZTF19aadyppr[a]	19abn	-14.73 ± 0.15	no	yes/no.	Sa	700	em	no	ILRT-gold
ZTF19acoaiub[a]	19udc	-14.62 ± 0.15	no	−/no	SAB(s)a	1250	em	no	ILRT-gold
ZTF19acdrkbh	19sfo	-14.62 ± 0.20	⋯	−/no	star-forming	600	em	no	ILRT-gold
ZTF19aagqkrq[a]	19ahd	-13.72 ± 0.15	no	−/no.	SA(s)cd	700	em	no	ILRT-gold
ZTF21aclzzex[a]	21adlx	-15.68 ± 0.16	no	yes/no	Sb	700	em	no	**ILRT-gold**
ZTF21abtduah[a]	21vdr	< -14.96	⋯	no/no	SB(s)d:	1300	no	no	ILRT-silver
ZTF21abfxjld	21prj	< -14.21	⋯	no/no.	star-forming	<300	no	no	ILRT-silver
ZTF18acrygkg	18lqq	< -14.14	no	−/no	SA(s)bc				ILRT-bronze
ZTF19aavwbxs	19fxy	-14.44 ± 0.17	no	−/no	star-forming				ILRT-bronze
ZTF19acpmbvd	19wbg	-14.66 ± 0.15	mp	yes/yes	SAB(r)a	1700			LBV?
ZTF20abwilhb	20swt	-13.87 ± 0.16	no.	no/no	Scd	3300	no	no	LBV/Type II?
ZTF21aagydmn	21bug	-14.36 ± 0.15	no	yes/no	SAd	2600	no	no	LBV?
ZTF21aantupk	21efb	-14.71 ± 0.15	no	−/yes	–				LBV/AGN?
ZTF21aclyyfm	21adlw	-16.03 ± 0.15	no	−/yes	SA(rs)b		no	no	LBV?
ZTF21aaitlhy	21afm	-15.44 ± 0.15	mp	yes/yes	SBb				LBV?
ZTF18aawoeho	21ahuh	-15.51 ± 0.15	no	no/no	starburst				?
ZTF20ablmyzj	20afdc	-15.95 ± 0.30	no	−/no	S				?
ZTF20acfxnmv	20afdd	-14.67 ± 0.15	⋯	−/no	SB(s)cd				?
ZTF20acivtfy	20afde	-13.72 ± 0.16	⋯	−/no	star-forming				?
ZTF21aapngrj	21gcg	-12.75 ± 0.15	no	−/no					?
ZTF21aakbdzz	21czz	-14.83 ± 0.10	no	−/no	S				?
ZTF21aamwyxf	21dtz	-15.98 ± 0.15	no	no/no	E				?

Notes. The "–" symbols and unfilled entries indicate instances for which data are not available.
[a] Events used for rate calculation in Section 3.
[b] Galaxy morphologies are taken from NED.
[c] Where multiple spectra are available, the maximum FWHM is reported.
[d] The molecular features are visible in spectra from the literature (see Section 2.2.2).

Spectrograph (HRS; Bramall et al. 2010). The NIR spectra were taken with the Near-Infrared Echelle Spectrograph (NIRES; $R \approx 2700$; Wilson et al. 2004) on the Keck II 10 m telescope and the Triplespec spectrograph ($R \approx 2500$; Herter et al. 2008) on P200. The log of the spectroscopic observations is listed in Table 2. In addition to these, we obtained several low-resolution ($R \approx 100$) spectra with the Spectral Energy Distribution Machine (SEDM; Blagorodnova et al. 2018; Rigault et al. 2019; Kim et al. 2022) on the 60 inch telescope at Palomar Observatory. These spectra are not discussed here, as their resolution is too low for a useful analysis. All of our spectra (including those having low resolution) will be made available online (Section 7).

LRNe, ILRTs, and LBV outbursts can have similar spectroscopic properties, especially at early times. However, some LBV eruptions have expansion velocities exceeding $\sim$2000 km s^{-1}, while LRNe and ILRTs have lower expansion velocities (typically $\sim$1000 km s^{-1}). The full width at half maximum (FWHM) intensity velocities of the Hα emission line in the transients with spectroscopic coverage are listed in Table 1. For transients with multiple spectra, the maximum velocity is listed. Early-time spectra of both LRNe and ILRTs are characterized by narrow Hα ($v_{FWHM} \leqslant 1000$ km s^{-1}) emission. [Ca II] emission was thought to be a defining feature of ILRTs; however, it was recently discovered that some LRNe can show [Ca II] emission (Cai et al. 2019), while some ILRTs do not exhibit [Ca II] at certain phases (Andrews et al. 2021). Late-time spectroscopic observations can help confidently distinguish between LRNe and ILRTs. In LRNe, Hα emission grows narrower and weaker

Table 2
Observation Log of Spectra Presented in This Paper

Name	Tel./ Inst.	Date	Resolution	Name	Tel./ Inst.	Date	Resolution
ZTF18abwxrhi	P200/DBSP	2018-9-18	1500	ZTF21aancgbm	Keck/NIRES	2021-4-18	1000
ZTF18abwxrhi	P200/DBSP	2018-10-10	1000	ZTF21aagppzg	Keck/NIRES	2021-4-18	1000
ZTF18acbwfza	Gemini/GMOS	2018-11-2	2000	ZTF21aaekeqd	Keck/LRIS	2021-5-09	750
ZTF18acbwfza	P200/DBSP	2018-11-2	1000	ZTF21abfxjld	Keck/LRIS	2021-7-6	750
ZTF18acbwfza	Keck/LRIS	2018-11-10	750	ZTF21abfxjld	Keck/LRIS	2021-8-14	750
ZTF18acdyopn	Keck/LRIS	2018-11-10	750	ZTF21abfxjld	Keck/NIRES	2021-9-25	1000
ZTF19aadyppr	P200/DBSP	2019-1-26	1000	ZTF21abtduah	P200/DBSP	2021-11-6	1000
ZTF19aagqkrq	NOT/ALFOSC	2019-2-11	350	ZTF21aclyyfm	P200/DBSP	2021-11-6	1000
ZTF19aagqkrq	P200/DBSP	2019-2-12	1000	ZTF21aclzzex	Shane/KAST	2021-11-12	1000
ZTF19aadyppr	NOT/ALFOSC	2019-2-23	350	ZTF21acpkzcc	Keck/NIRES	2021-11-17	1000
ZTF19aadyppr	Keck/LRIS	2019-3-7	750	ZTF21acpkzcc	SALT/HRS	2021-11-29	15000
ZTF19aadyppr	P200/DBSP	2019-3-16	1000	ZTF21acpkzcc	P200/DBSP	2021-12-1	1000
ZTF19aadyppr	P200/DBSP	2019-4-13	1000	ZTF21abtduah	P200/DBSP	2021-12-1	1000
ZTF19aadyppr	P200/DBSP	2019-5-13	1000	ZTF21aclzzex	P200/DBSP	2021-12-1	1000
ZTF19acdrkbh	Keck/LRIS	2019-10-27	750	ZTF21aagppzg	P200/TSpec	2021-12-12	1000
ZTF19acoaiub	P200/DBSP	2019-11-5	1000	ZTF21acpkzcc	P200/DBSP	2022-1-12	1000
ZTF19acoaiub	Keck/NIRES	2019-12-4	1000	ZTF21acpkzcc	P200/TSpec	2022-1-20	1000
ZTF19acpmbvd	LT/SPRAT	2019-12-23	350	ZTF21aclzzex	Keck/LRIS	2022-1-26	750
ZTF20aawdwch	NOT/ALFOSC	2020-5-15	300	ZTF21aclyyfm	P200/DBSP	2022-2-2	1000
ZTF20abwilhb	Keck/LRIS	2020-10-20	750	ZTF21aancgbm	Keck/LRIS	2022-2-3	750
ZTF21aagppzg	P200/DBSP	2021-2-8	1000	ZTF21acpkzcc	Keck/LRIS	2022-2-3	750
ZTF21aaekeqd	Keck/LRIS	2021-2-17	750	ZTF21abtduah	Keck/LRIS	2022-2-3	750
ZTF21aagppzg	P200/DBSP	2021-2-20	1000	ZTF21aclzzex	Keck/LRIS	2022-3-1	750
ZTF21aagydmn	P200/DBSP	2021-2-20	1000	ZTF21abtduah	Keck/LRIS	2022-3-3	750
ZTF21aagppzg	LT/SPRAT	2021-3-19	350	ZTF21aclzzex	Keck/LRIS	2022-3-3	750
ZTF21aancgbm	P200/DBSP	2021-4-9	1000	ZTF21aagppzg	Keck/NIRES	2022-3-16	1000
ZTF21aagppzg	P200/DBSP	2021-4-9	1000	ZTF21aancgbm	Keck/NIRES	2022-3-17	1000
ZTF21aaekeqd	Keck/LRIS	2021-4-14	750	ZTF21aclzzex	Keck/NIRES	2022-3-17	1000
ZTF21aaekeqd	Keck/NIRES	2021-4-18	1000	ZTF21aclzzex	Keck/NIRES	2022-4-15	1000

with time since peak brightness, disappears, and eventually re-emerges (Blagorodnova et al. 2020). Late-time spectra of LRNe also exhibit molecular absorption features. In contrast, ILRTs have persistent narrow H emission throughout their evolution. Their late-time spectra do not show molecular features, but they have strong Hα and Ca II emission lines.

Provided that not all of our sources have late-time spectroscopic coverage, we use the available spectra (from the literature wherever necessary) together with the light curves to create a classification scheme for these transients. We classify the 34 transients into eight categories: Possible LBV outbursts, LRN-gold, LRN-silver, LRN-bronze, ILRT-gold, ILRT-silver, ILRT-bronze, and Ambiguous. We describe these categories in detail below. Briefly, for LRNe and ILRTs, the gold sample comprises transients that we can confidently classify in either category, the silver sample comprises transients that have photometry and spectra indicative of their class but lack smoking-gun signatures associated with the class, and the bronze category comprises transients that have photometric evolution similar to their class but do not have any spectroscopic data. The "Ambiguous" category consists of seven sources that have poor-quality data (no spectra *and* low-quality sparse photometric coverage owing to bad weather or solar conjunction of the transient), rendering us unable to place them in any of the other categories. Table 1 lists the classification of these sources based on this scheme. We describe the sources in each category below.

2.2.1. Possible LBV Eruptions

This category includes sources that show broad ($v_{\rm FWHM} \geqslant 2000$ km s^{-1}) Hα emission in their spectra *or* have historic outbursts in archival data. A total of six transients in our short list satisfy these criteria. Two of these (ZTF 21aagydmn and ZTF 20abwilhb) show broad Hα emission with FWHM velocities of 2600 and 3300 km s^{-1} and are likely LBV outbursts. The ATLAS and PTF data classify four additional sources as potential LBVs (ZTF 19acpmbvd, ZTF 21aantupk, ZTF 21aclyyfm, and ZTF 21aaitlhy). We describe these sources in Appendix.

2.2.2. LRN-gold

This category includes six spectroscopically confirmed LRNe detected in ZTF data in the last three years. Three of these have been studied in detail previously: ZTF 18acbwfza (AT 2018hso; Cai et al. 2019), ZTF 19adakuot (AT 2019zhd; Pastorello et al. 2021a), and ZTF 20aawdwch (AT 2020hat; Pastorello et al. 2021b). Three other transients—ZTF 21aancgbm (AT 2021biy; Cai et al. 2022), ZTF 21aagppzg (AT 2021blu; Pastorello et al. 2022), and ZTF 21acpkzcc (AT 2021aess; Davis et al. 2021)—were identified as possible LRNe in 2021. We initiated optical and NIR photometric and spectroscopic follow-up campaigns for these objects, which confirmed their nature as LRNe.

Our light curves of these transients are shown in Figure 1. For all our calculations, we use host-galaxy redshifts corrected for local velocity flows from the NASA Extragalactic Database

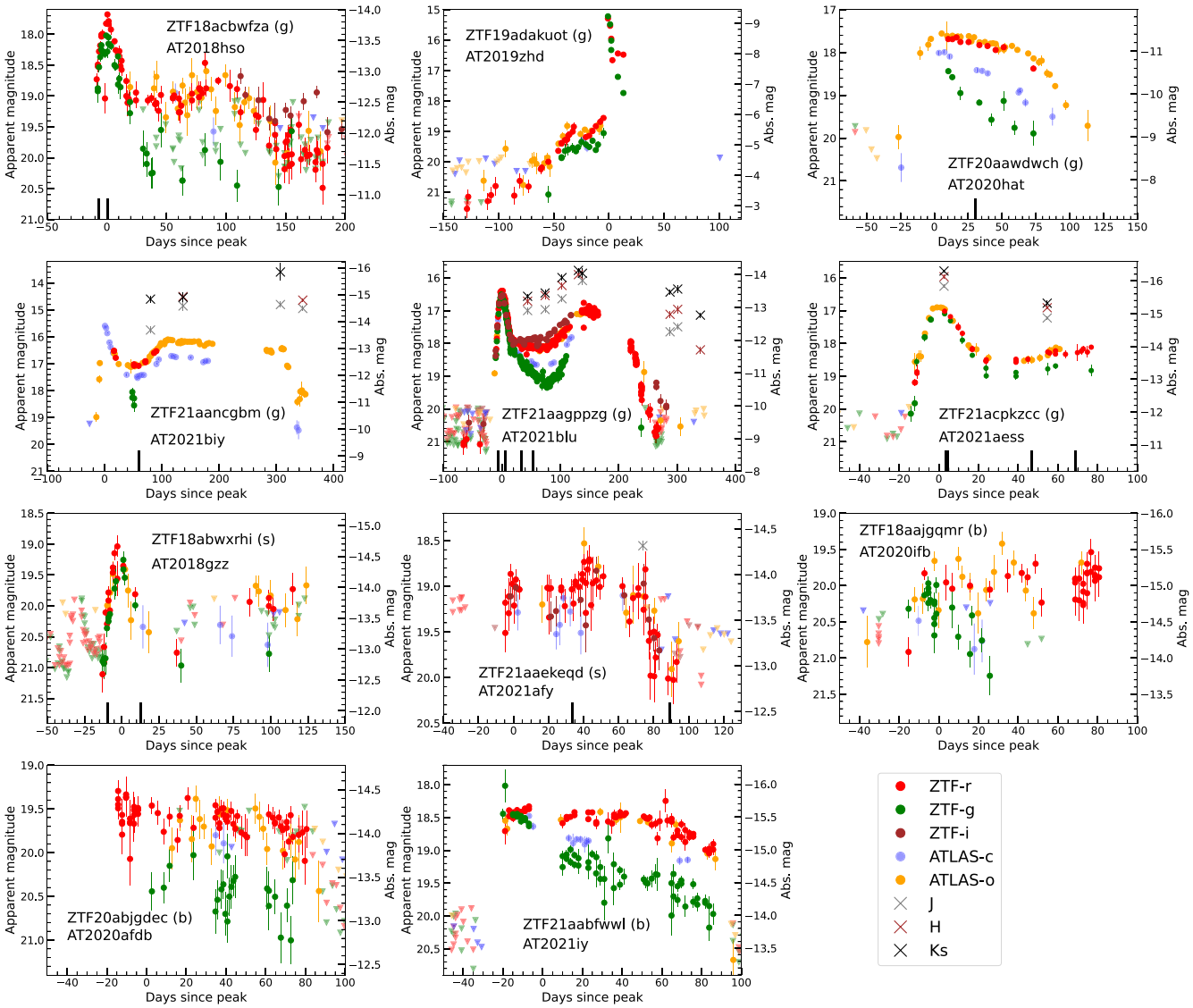

Figure 1. Forced-photometry light curves of the 11 LRNe in our sample. The transients in the gold, silver, and bronze samples are marked in parentheses with "*g*," "*s*," and "*b*" (respectively). The ZTF-*g*, ZTF-*r*, ZTF-*i*, ATLAS-*c*, and ATLAS-*o* data are plotted as green, red, brown, blue, and orange points, respectively. The *J*, *H*, and K_s magnitudes are plotted as gray, brown, and black crosses, respectively. Downward-pointing triangles indicate 5σ upper limits. Days are in the observer frame. The light curves have been corrected for extinction using the values listed in Table 3. Solid black vertical lines indicate epochs at which spectra were obtained.

(NED), and assume $H_0 = 73$ km s^{-1} Mpc^{-1}. We use Milky Way line-of-sight extinction values from Schlafly et al. (2012). Host-galaxy extinctions for LRNe are calculated using Na I D equivalent widths in their early-time spectra (see discussion of individual objects below). We calculate the peak magnitudes and epoch of maximum brightness by fitting polynomials to the near-peak light curve. We calculate the pseudobolometric light curves by fitting blackbodies to the available optical data. The derived photometric properties and the adopted distances and extinctions for the LRNe in our sample are listed in Table 3.

Our spectra of these transients are shown in Figures 2 and 3. We analyze the optical spectra and derive the hydrogen Balmer line velocities by fitting Lorentzian profiles (which are better fits than Gaussian profiles) and corrected the velocities for instrumental broadening. We also measure the Balmer decrement (β) as the ratio of Hα to Hβ line fluxes in the spectra where both lines are detected. The spectroscopic properties are listed in Table 4. We now briefly describe individual members of our sample.

1. ZTF 18acbwfza (AT 2018hso) is located in the star-forming galaxy NGC 3729. Our earliest spectrum (7 days before peak brightness) shows Na I D absorption with an equivalent width of 1.5 ± 0.4 Å. Assuming this gas is associated with dust in the interstellar medium, and using the correlation from Turatto et al. (2003), we derive $E(B-V)_{\rm host} = 0.23 \pm 0.06$ mag. This is consistent with the value used by Cai et al. (2019). The light curve is characteristic of LRNe, with an early blue peak lasting for ∼20 days, followed by a prolonged plateau where the transient evolves rapidly to redder colors. We note that the transient shows signs of evolving back to bluer colors at late times, when the *r*-band light curve is declining but the *g*-band light curve has plateaued. However, we caution that the *g*-band detections at this phase from ZTF have low significance (3σ). Our spectra sample only the first blue peak, and they show strong Balmer emission lines with $v_{\rm FWHM} \approx 500$ km s^{-1}. These spectra also exhibit narrow Ca II NIR triplet lines with a P Cygni profile. The absorption of the P Cygni profile extends to a maximum

Table 3
Photometric Properties of LRN and ILRTs[a]

Name	DM[b] (mag)	$E(B-V)$[c] (mag)	$m_{r,\mathrm{peak}}$ (mag)	$M_{r,\mathrm{peak}}$ (mag)	$\mathrm{MJD_{peak}}$ (d)	L_{peak} (erg $\mathrm{s^{-1}}$)
ZTF18acbwfza	31.60	0.250	18.47 ± 0.02	-13.82 ± 0.15	58430.9 ± 0.2	$9.3^{+0.3}_{-0.3} \times 10^{40}$
ZTF19adakuot	24.45	0.055	15.00 ± 0.01	-9.60 ± 0.15	58891.6 ± 0.1	$2.0^{+0.1}_{-0.1} \times 10^{39}$
ZTF20aawdwch	28.97	0.093	17.79 ± 0.02	-11.43 ± 0.15	58963.0 ± 1.2	$>1.2 \times 10^{40}$
ZTF21aagppzg	29.90	0.020	16.45 ± 0.01	-13.50 ± 0.15	59258.9 ± 0.1	$7.9^{+0.1}_{-0.1} \times 10^{40}$
ZTF21aancgbm	29.43	0.261	16.28 ± 0.03	-13.86 ± 0.15	59252.9 ± 0.5	$>8.9 \times 10^{40}$
ZTF21acpkzcc	32.09	0.032	17.05 ± 0.03	-15.12 ± 0.15	59545.5 ± 0.2	$3.3^{+0.2}_{-0.2} \times 10^{41}$
ZTF18abwxrhi	33.70	0.047	19.33 ± 0.06	-14.50 ± 0.16	58386.2 ± 0.9	$1.9^{+1.5}_{-0.3} \times 10^{41}$
ZTF21aaekeqd	32.87	0.330	19.82 ± 0.06	-13.95 ± 0.16	59229.2 ± 1.6	$6.0^{+6.4}_{-4.6} \times 10^{41}$
ZTF18aajgqmr	35.00	0.018	19.69 ± 0.09	-15.36 ± 0.17	58969.7 ± 1.0	$3.3^{+0.7}_{-0.4} \times 10^{41}$
ZTF20abjgdec	33.78	0.141	19.80 ± 0.06	-14.37 ± 0.16	59045.6 ± 2.1	$2.4^{+13.3}_{-1.2} \times 10^{41}$
ZTF21aabfwwl	33.99	0.043	18.39 ± 0.05	-15.72 ± 0.16	59239.5 ± 1.8	$5.2^{+1.1}_{-0.7} \times 10^{42}$
ZTF18acdyopn	33.92	0.064	19.76 ± 0.11	-14.33 ± 0.19	58426.8 ± 2.4	$2.2^{+21.7}_{-1.0} \times 10^{41}$
ZTF19aadyppr	29.45	0.705	16.65 ± 0.01	-14.73 ± 0.15	58534.7 ± 0.5	$2.3^{+0.1}_{-0.1} \times 10^{41}$
ZTF19acoaiub	31.83	0.038	17.31 ± 0.02	-14.62 ± 0.15	58799.1 ± 0.1	$2.0^{+0.2}_{-0.2} \times 10^{41}$
ZTF19acdrkbh	34.33	0.051	19.85 ± 0.12	-14.62 ± 0.20	58764.3 ± 1.9	$1.8^{+0.9}_{-0.4} \times 10^{41}$
ZTF19aagqkrq	30.76	0.200	17.58 ± 0.03	-13.72 ± 0.15	58538.3 ± 1.1	$8.0^{+0.5}_{-0.4} \times 10^{40}$
ZTF21aclzzex	33.89	0.019	18.26 ± 0.06	-15.68 ± 0.16	59528.6 ± 1.7	$5.2^{+3.7}_{-1.2} \times 10^{41}$
ZTF21abtduah	33.22	0.022	<18.31	$< -14.96 \pm 0.15$	<59522.5	$>1.3 \times 10^{41}$
ZTF21abfxjld	33.43	0.106	<19.51	$< -14.21 \pm 0.20$	<59359.8	$>8.0 \times 10^{40}$
ZTF19aavwbxs	33.26	0.038	18.92 ± 0.08	-14.44 ± 0.17	58644.7 ± 8.1	$2.2^{+0.6}_{-0.3} \times 10^{41}$
ZTF18acrygkg	33.35	0.036	$<19.31.$	$< -14.14 \pm 0.16$	<58447.5	

Notes.
[a] The two classes LRN and ILRT are separated by a horizontal line.
[b] The distance moduli have uncertainties of 0.15 mag and are taken from NED.
[c] Galactic extinction values are taken from Schlafly & Finkbeiner (2011); host-galaxy extinction is calculated as described in the text.

velocity $v_{\mathrm{max}} \approx 400$–$500\ \mathrm{km\ s^{-1}}$. Cai et al. (2019) report weak [Ca II] in this transient. We find marginal evidence for [Ca II] emission in only one of our spectra, taken 1 day post peak. Late-time spectra from Cai et al. (2019) show strong molecular absorption features.

2. ZTF 19adakuot (AT 2019zhd) is located in M31. Following Pastorello et al. (2021a), we assume that the total extinction is dominated by the Milky Way. The transient has the lowest luminosity in our sample (peaking at $M_r \approx -9.5$ mag). We do not have any spectroscopic data for this transient, but late-time spectra presented by Pastorello et al. (2021a) show molecular absorption features.

As noted by Pastorello et al. (2021a), this transient shows precursor activity for a few months leading up to the explosion. In these months, the field of ZTF 19adakuot was imaged with the ZTF camera several times per night. We stack the ZTF forced photometry from images taken on the same night; this allows us to recover several additional detections beyond the ones reported by Pastorello et al. (2021a), which are plotted in Figure 4. We further bin the photometry in bins of 10 days, to increase the significance of the detections. The ZTF detections date back to 160 days before the r-band peak, when the transient was first detected at $m_r \approx 22.7 \pm 0.3$ mag. The binned ZTF light curve shows that the transient went through a gradual, bumpy brightening phase for ∼160 days before the main explosion. Three bumps can be identified in the r-band light curve, each with a duration of ∼50 days. During each of these bumps, the transient brightens by an increasing amount (∼0.5, 1, and 2.5 mag, respectively) before plateauing or declining by a modest amount (∼0.5 mag) at the end of each bump. After the third bump, the transient brightens gradually by ∼1 mag for 25 days before brightening rapidly by 4 mag as it transitions into the main explosion. This bumpy rise is reminiscent of the pre-outburst evolutions of M31-LRN-2015 (Blagorodnova et al. 2020), V838 Mon (Munari et al. 2002; Tylenda 2005), and AT 2020hat (Pastorello et al. 2019b).

At the end of the first bump (MJD 58759), fitting a single blackbody to the g and r detections suggests a source with $T_{\mathrm{eff}} = 6600^{+2400}_{-1600}$ K, a radius $R = 17^{+14}_{-7}\ R_\odot$, and a luminosity of $5.5^{+1.3}_{-0.7} \times 10^2\ L_\odot$. This photosphere is most likely formed by mass outflowing from the outer Lagrangian (L2) point (see, e.g., Pejcha et al. 2017 or MacLeod et al. 2022). On the second bump, the transient is only detected in r, with the most constraining g-band upper limit giving $g - r > 0.8$ mag, suggesting that the optically thick photosphere has cooled. This likely continues up to the beginning of the third bump on MJD 58837, where the temperature has cooled down to $T = 3900^{+700}_{-700}$ K, the photosphere has expanded to $R = 170^{+140}_{-70}\ R_\odot$, and $L = 6.1^{+3.9}_{-1.7} \times 10^3\ L_\odot$. This would imply a photospheric expansion speed of ∼10–30 $\mathrm{km\ s^{-1}}$. After this, the temperature increases quickly in the next 12 days on the third bump to 5700^{+300}_{-300} K with $L = 7.5^{+0.3}_{-0.3} \times 10^3\ L_\odot$, and reduced $R = 90^{+12}_{-12}\ R_\odot$ on MJD 58849, suggesting the temperature increase was accompanied by a drop in opacity. This is followed by a surprisingly sharp decline in the redder (r, o) bands but a slow brightening in g. During this decline, the temperature increases to 6900^{+1100}_{-1000} K but the radius drops to $69^{+27}_{-16}\ R_\odot$ with an increased luminosity of $9.5^{+0.8}_{-0.6} \times 10^3\ L_\odot$ on MJD 58871. This is followed by an increase in luminosity and

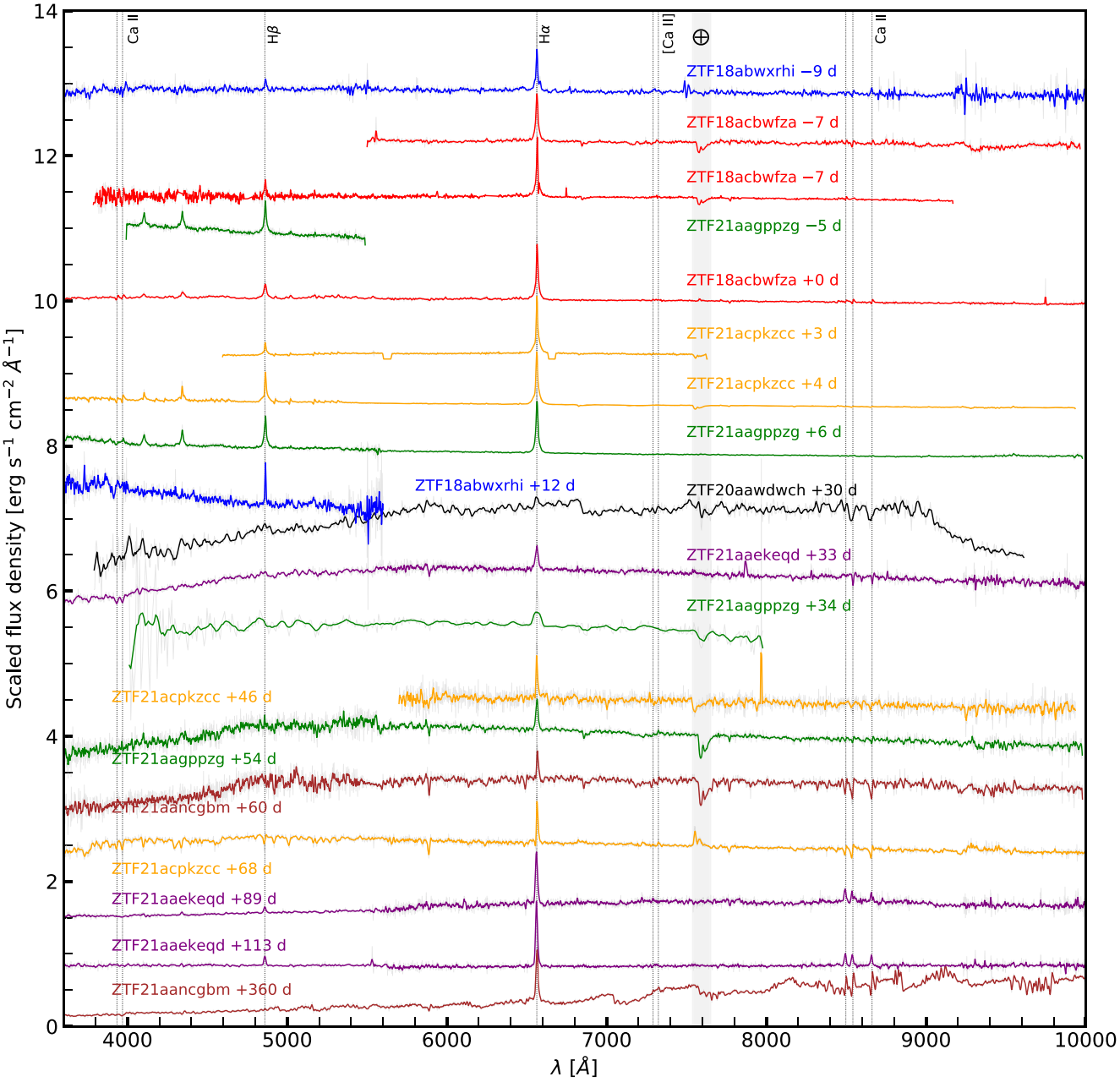

Figure 2. Optical spectra of LRNe presented in this paper. In plots of spectra throughout, we indicate the locations of telluric features with an "Earth" symbol.

photospheric radius accompanied by a slight decrease in temperature, to $L = 1.7^{+0.2}_{-0.1} \times 10^4\,L_\odot$ on MJD 58887. In the next five days, the transient brightens rapidly to its peak luminosity of $\sim 5.2 \times 10^5\,L_\odot$.

A full analysis of this complex precursor photometric evolution is outside the scope of this paper. A possible explanation for the abrupt temperature increases in this final phase is shocks owing to collisions within the L2 stream, as suggested by Pejcha et al. (2017). The total energy radiated during this ∼40 day duration is $\sim 10^{44}$ erg. Assuming an L2 velocity of 30 km s^{-1}, the mass required in the L2 stream is $\geqslant 10^{-2}\,M_\odot$.

3. ZTF20aawdwch (AT 2020hat) is located in NGC 5068. We follow Pastorello et al. (2021b) and assume that the extinction is dominated by the Milky Way. The ZTF light curve samples the post-peak decline, starting at $m_r = 17.90 \pm 0.06$ mag. Our sole spectrum was taken at a phase of 30 days since peak, which shows a reddened continuum, extremely weak Hα emission, some broad but weak molecular absorption features, and Ca II NIR triplet absorption lines—characteristic of LRNe on the red plateau phase. Molecular absorption features are clearly detected in late-time spectra presented by Pastorello et al. (2021b).

4. ZTF 21aancgbm (AT 2021biy, Smith et al. 2021a; Cai et al. 2022) is located in the galaxy NGC 4631. We do not have spectra at early phases, so we adopt the host extinction derived by Cai et al. (2022) using Na I D absorption. The light curve is characteristic of LRNe, with an initial blue peak lasting for ∼50 days, followed by a rebrightening and a prolonged red plateau of ∼350 days. The field of ZTF 21aancgbm is not part of the regular 2 day cadence ZTF survey, so the ZTF data sample only a small portion of the light curve. We combine the

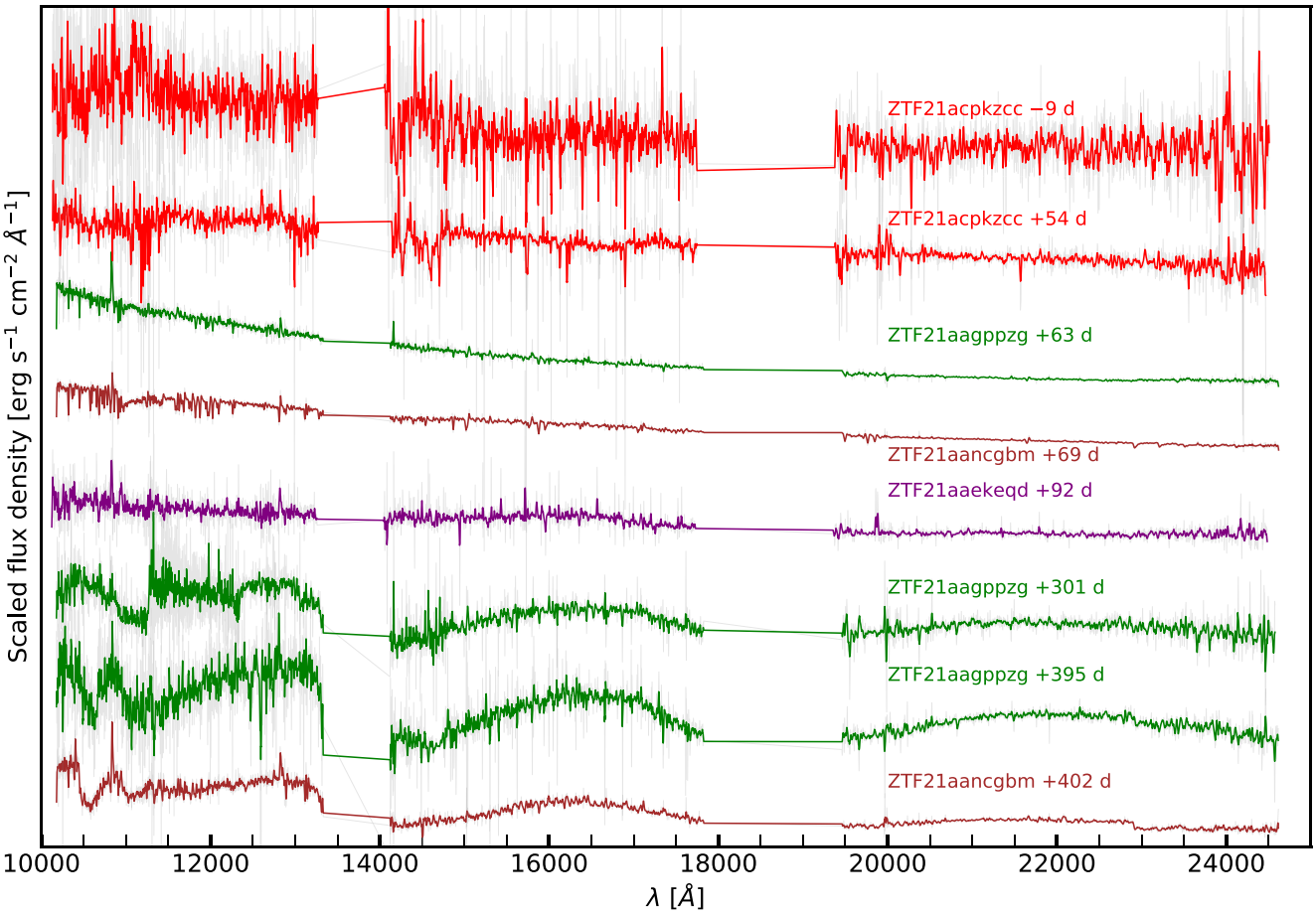

Figure 3. NIR spectra of LRNe presented in this paper.

ZTF data with ATLAS data, which shows that the light curve lasts for more than 400 days and is the longest-duration LRN in our sample.

We obtained JHK_s NIR imaging with P200/WIRC on several epochs on the plateau, which shows that the transient was significantly brighter in the NIR bands (by >1 mag) than in the optical (see Figure 1). The transient shows a late-time bump once it falls off the plateau, likely the result of collision with circumstellar matter (CSM) as noted by Cai et al. (2022). Our spectroscopic coverage comprises two optical spectra at +60 and +360 days since peak, and two NIR spectra at +69 and +402 days since peak. The +60 day spectrum shows a reddened continuum with weak, unresolved Hα emission ($v_{\rm FWHM} \approx 350$ km s^{-1}) and the Ca II NIR triplet with P Cygni line profiles ($v_{\rm max} \approx 400$ km s^{-1}). We also detect weak [Ca II] lines with P Cygni line profiles. The +69 days NIR spectrum shows several metallic absorption lines, as well as the CO absorption bandhead. The very late-time optical spectrum at +360 days shows a highly reddened continuum with several strong molecular absorption features of TiO and VO, confirming the classification as an LRN. This spectrum also shows strong, narrow Hα emission (with increased $v_{\rm FWHM} \approx 500$ km s^{-1}) and Ca II NIR lines with P Cygni profiles ($v_{\rm max} \approx 600$ km s^{-1}).

The light-curve shape and long duration of ZTF 21aancgbm make it an interesting member of the LRN family. The 200 day plateau resembles that seen in SNe IIP, and it is tempting to posit that it is powered by hydrogen recombination. Matsumoto & Metzger (2022) provide scaling relations between the plateau luminosity ($L_{\rm pl}$), duration ($t_{\rm pl}$), and ejected mass ($M_{\rm ej}$) for a recombination-powered LRN plateau, given by

$$M_{\rm ej} \approx 1.6\, f_{\rm ad,\,0.3}^{-1} \left(\frac{t_{\rm pl}}{100\ {\rm days}}\right)\left(\frac{L_{\rm pl}}{10^{39}\ {\rm erg\ s^{-1}}}\right) M_\odot, \qquad (1)$$

where $f_{\rm ad,0.3} \approx 1$ is a dimensionless factor quantifying inefficiencies in radiating the recombination energy. The plateau is defined as the duration between the point where the transient begins rebrightening after the first blue peak to the time when it falls off the plateau to the same brightness. We calculate an average plateau luminosity $L_{\rm pl} \approx 2.3 \times 10^{40}$ erg s^{-1} and a plateau duration $t_{\rm pl} \approx 274$ days. This suggests a recombining ejecta mass of $\sim 100\, M_\odot$ for this LRN, implying an extremely massive progenitor. This seems unlikely, given that the correlation between peak luminosity and progenitor mass for LRNe (Blagorodnova et al. 2021) predicts a primary progenitor mass in the range $\sim$10–50 $M_\odot$. Additionally, archival Hubble Space Telescope (HST) imaging Cai et al. (2019) suggests a progenitor mass of $\sim$17–24 $M_\odot$. It is therefore very likely that the plateau luminosity is too high to be explained by H recombination alone. A plausible source of additional energy is shock interaction between the merger ejecta and pre-existing material around the binary that was ejected during the CE phase. Following Matsumoto & Metzger (2022), assuming that only the timescale but not the luminosity of the transient is set

Table 4
Spectroscopic Properties of LRN and ILRTs

Name	MJD (d)	Phase (d)	$v^a_{\mathrm{H}\alpha,\mathrm{FWHM}}$ (km s^{-1})	$v^a_{\mathrm{H}\beta,\mathrm{FWHM}}$ (km s^{-1})	β
			LRNe		
ZTF18acbwfza	58424	−7.1	510 ± 60		
ZTF18acbwfza	58424	−7.1	450 ± 30	750 ± 60	2.1 ± 0.1
ZTF18acbwfza	58432	+0.9	350 ± 40	760 ± 120	2.2 ± 0.2
ZTF18abwxrhi	58379	−9.3	280 ± 40	250 ± 120	3.8 ± 0.7
ZTF21aaekeqd	59262	+33.4	650 ± 20		
ZTF21aaekeqd	59318	+89.3	340 ± 30	260 ± 70	2.1 ± 0.2
ZTF21aaekeqd	59343	+113.8	300 ± 20	<370	7.6 ± 0.6
ZTF21aagppzg	59253	−5.9	490 ± 60	760 ± 100	2.5 ± 0.2
ZTF21aagppzg	59265	+6.1	420 ± 40	700 ± 80	2.7 ± 0.2
ZTF21aagppzg	59313	+54.1	500 ± 60		
ZTF21aancgbm	59313	+60.1	<350		
ZTF21aancgbm	59613	+360.1	460 ± 40		
ZTF21acpkzcc	59549	+4.6	470 ± 50	540 ± 70	3.7 ± 0.3
ZTF21acpkzcc	59591	+46.6	<340		
ZTF21acpkzcc	59613	+68.6	<300		
			ILRTs		
ZTF18acdyopn	58432	+5.1	300 ± 40	630 ± 120	3.3 ± 0.4
ZTF19aadyppr	58509	−25.7	330 ± 50	<250	2.5 ± 0.3
ZTF19aadyppr	58526	−8.7	640 ± 80	680 ± 180	2.4 ± 0.4
ZTF19aadyppr	58537	+2.2	470 ± 170	2400 ± 850	0.9 ± 0.3
ZTF19aadyppr	58549	+14.3	530 ± 120		
ZTF19aadyppr	58558	+23.2	710 ± 180		
ZTF19aadyppr	58586	+51.3	400 ± 70		
ZTF19aadyppr	58616	+81.3	330 ± 40		
ZTF19acoaiub	58792	−7.1	1250 ± 300	2000 ± 850	3.4 ± 1.1
ZTF19acdrkbh	58783	+18.7	590 ± 80		
ZTF19aagqkrq	58525	−13.4	<850	1000 ± 200	2.3 ± 0.3
ZTF19aagqkrq	58526	−12.4	670 ± 50	2000 ± 500	1.6 ± 0.2
ZTF21aclzzex	59530	+1.9	670 ± 60	1200 ± 180	3.5 ± 0.5
ZTF21aclzzex	59605	+76.9	500 ± 60	380 ± 110	5.5 ± 1.9
ZTF21aclzzex	59639	+110.3	550 ± 40	300 ± 70	7.9 ± 0.9
ZTF21abtduah	59524	+1.5	1170 ± 100		
ZTF21abtduah	59549	+26.5	1290 ± 100		
ZTF21abtduah	59613	+90.5	870 ± 30	690 ± 70	8.4 ± 0.6
ZTF21abtduah	59641	+118.5	770 ± 30	780 ± 60	10.6 ± 0.6
ZTF21abfxjld	59401	+41.7	<290	<250	3.6 ± 0.5
ZTF21abfxjld	59440	+80.2	<270	<260	4.6 ± 0.4

Notes. The velocities have been corrected for instrumental resolutions listed in Table 2. Upper limits are reported for unresolved lines.

by H recombination, the required recombining ejected mass is

$$t_{\mathrm{pl}} \approx 140\ \rho_{i,-11}^{-1/3} \left(\frac{M_{\mathrm{ej}}}{M_\odot}\right)^{1/3} \left(\frac{v_{\mathrm{E}}}{300\ \mathrm{km\ s^{-1}}}\right)^{-1} \mathrm{days}, \quad (2)$$

where v_{E} is the mean ejecta velocity and $\rho_{i,-11} = \rho_i/10^{-11}$ g cm$^{-3} \approx 1$ and ρ_i is the characteristic density at which the recombination completes. We adopt $v_{\mathrm{E}} \approx 430$ km s^{-1} from Cai et al. (2022), which gives $M_{\mathrm{ej}} \approx 22\,M_\odot$. This value is larger than that derived by Cai et al. (2022), owing to the larger plateau duration that we have assumed. Assuming that this ejected mass runs into pre-existing matter ($M_{\mathrm{pre}} \ll M_{\mathrm{ej}}$) with velocity $v_{\mathrm{pre}} \ll v_{\mathrm{E}}$, the generated shock luminosity can be written as (Matsumoto & Metzger 2022)

$$L_{\mathrm{pl}}^{\mathrm{sh}} \approx 7 \times 10^{39}\ \rho_{i,-11}^{-1/3} \left(\frac{M_{\mathrm{pre}}}{0.1 M_{\mathrm{ej}}}\right) \left(\frac{v_E}{300\ \mathrm{km\ s^{-1}}}\right)^3 \times \left(\frac{M_{\mathrm{ej}}}{M_\odot}\right)^{2/3} \mathrm{erg\ s^{-1}}. \quad (3)$$

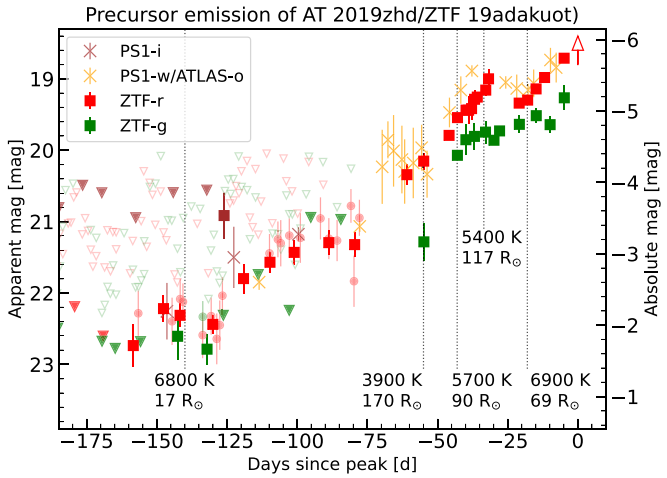

Figure 4. Pre-explosion g, r, and i detections for ZTF 19adakuot. For phases < -75 days, we bin the ZTF flux measurements taken on the same day, to increase the sensitivity. These points are plotted as faint background circles. We further bin these measurements in bins of 10 days, to increase their significance. The binned measurements are showed as solid squares. For phases > -75 days, the squares represent ZTF forced photometry from single visits. The triangles denote 5σ upper limits. The crosses show measurements reported previously by Pastorello et al. (2021a). At the epochs marked by the dotted vertical lines, we indicate the effective temperatures and photospheric radii to demonstrate the dramatic variations exhibited by the precursor (see text). The initial pre-explosion behavior is consistent with photosphere L2 mass loss forming an optically thick photosphere detectable by ZTF at ~ -150 days, which expands and cools up to ~ -70 days. Further collisions in the L2 stream or accretion onto the companion star can cause sudden increases in temperature over the next 70 days, until the transient brightens rapidly and transitions to the main explosion (marked by the red arrow).

The observed plateau luminosity can be explained by shock interactions from Equations (2) and (3) if $M_{\rm pre} \approx 0.3\,M_{\odot}$. We note that the assumption $M_{\rm pre} \ll M_{\rm ej}$ may not be valid, as the binary can lose a few solar masses prior to the LRN event (Blagorodnova et al. 2021). Nevertheless, these mass estimates demonstrate that strong CSM interaction can plausibly explain the high luminosities of this transient. Given the very late-time bump in the light curve of this LRN, it is not unreasonable to expect significant CSM around the binary, providing a plausible explanation for its plateau. The CSM interaction could also be in the form of collimated outflows interacting with previously ejected spherical shells, as suggested for some other LRNe by Soker & Kaplan (2021) and Soker (2020).

5. ZTF 21aagppzg (AT 2021blu, Smith et al. 2021b; Pastorello et al. 2022) is located on the outskirts of the galaxy UGC 5829. It was first classified as an LBV outburst (Uno et al. 2021); however, our late-time NIR spectra show strong molecular absorption features, indicating that this is an LRN. We adopt the extinction to be dominated by the Milky Way, as our early-time optical spectra do not show any strong DNa I absorption lines.

The light curve is characteristic of LRNe and shows two pronounced peaks—an initial blue peak for ∼50 days, followed by a second red peak lasting ∼200 days. Unlike ZTF 21aancgbm, the second peak does not show a plateau but has a smooth rise and decline. The P200/WIRC NIR photometry indicates that ZTF 21aagppzg was also significantly brighter in the NIR than in the optical. In particular at late times when the transient has faded below ZTF detection limits in r (>21 mag), it continues to be detected at ∼17 mag in the K band (see Figure 1). We stack the ZTF forced photometry prior to the outburst in bins of 5 days and recover some archival detections. The first detection in r is ∼1040 days prior to peak brightness with $m_r = 22.3 \pm 0.2$ mag. The transient was detected again at four epochs in r and g between 400 and 300 days before peak, at roughly constant magnitudes of $m_r = 22.4 \pm 0.3$ and $m_g = 22.5 \pm 0.3$. Finally, it is detected again 95 days before peak at $m_r = 21.8 \pm 0.3$ mag, brightens to $m_r = 20.9 \pm 0.2$ mag 65 days before peak, and fades back to $m_r = 21.9 \pm 0.3$ mag at 27 days before peak. It is also detected in the i band during this time period, with $m_i = 21.0 \pm 0.3$ mag.

Our spectroscopic coverage comprises four optical spectra at −5, +6, +34, and +54 days since peak brightness and three NIR spectra at +63, +301, and +395 days since peak. The two early-time optical spectra are characterized by a hot blue continuum with strong Balmer emission lines. The Hα emission line has $v_{\rm FWHM} \approx 500$–600 km s^{-1}. The Hβ line profile appears to be a superposition of a broad component with a narrow component; however, our spectral resolution is not sufficient to distinguish between the two. These spectra do not show the Ca II NIR triplet lines. The third optical spectrum has lower resolution and a lower signal-to-noise ratio (S/N). It shows a reddened continuum, with Hα being the only prominent feature. The final optical spectrum was obtained two months post peak and reveals a reddened continuum. The strength and velocity of the Balmer emission decreased, the Hα line developed a double-peaked profile, and Hβ is not detected. This spectrum also shows weak Ca II NIR triplet absorption lines, along with a forest of metallic absorption lines. The NIR spectrum at +63 days exhibits hydrogen emission lines with some metallic absorption lines. Our two final late-time NIR spectra show strong molecular absorption features of TiO, VO, and H_2O.

Similarly to the case of ZTF 21aancgbm, here we can use scaling relations to determine the ejecta masses. We estimate a median luminosity on the red plateau $L_{\rm pl} \approx 1.6 \times 10^{40}$ erg s^{-1} and a plateau duration $t_{\rm pl} \approx 180$ days. Using $v_{\rm E} \approx 500$ km s^{-1} and Equation (2) gives the recombining ejecta mass $M_{\rm ej} \approx 10\,M_{\odot}$, although the estimate is very sensitive to the assumed ejecta velocity. Again similarly to ZTF 21aancgbm, here recombination alone is not sufficient to explain the luminosity of the plateau, and Equation (3) implies interaction with pre-existing mass $M_{\rm pre} \approx 0.2\,M_{\odot}$. Pastorello et al. (2022) discuss archival HST and ground-based imaging of this transient, and the properties of the putative progenitor. We note that, in addition to the data presented in their paper, this transient has archival Spitzer Space Telescope/IRAC imaging from 2007 December 27. We detect a marginal source at the location of the transient with $m_{3.6} = 20.48 \pm 0.16$ mag and $m_{4.5} = 19.79 \pm 0.21$ mag (Vega system). We leave a more detailed analysis of this LRN and its progenitor properties to a future study.

6. ZTF 21acpkzcc (AT 2021aess) is the most luminous LRN in our sample, with peak $M_{\rm r} = -15.12 \pm 0.15$ mag. We do not identify strong Na I D in our early-time spectra, although this is possibly due to low S/N. We assume that the extinction is dominated by the Milky Way, but caution that extinction from the host galaxy could increase the peak-luminosity estimates for this transient. Similarly to those of the other LRNe described above, the light curve here shows two distinct peaks: a blue initial peak lasting ∼40 days, followed by a reddened plateau. However, our photometric coverage stops at ∼50 days

into the plateau, as the transient experienced solar conjunction. Similarly to the previous two LRNe, ZTF 21acpkzcc is brighter in the NIR (by >1 mag) than in the optical bands. Stacking the archival ZTF light curve in bins of 3 days shows some archival detections ∼70 days before peak at $m_g = 21 \pm 0.3$ and $m_r = 21.1 \pm 0.3$ mag. Our spectroscopic coverage comprises three optical spectra at +4, +46, and +68 days since peak brightness and one NIR spectrum at +54 days since peak. The early-time spectra show narrow Hα with $v_{\rm FWHM} \approx 500$ km s^{-1}, which grows weaker and narrower with time (FWHM <350 km s^{-1} at 46 days). The +68 day spectrum exhibits a weak P Cygni profile for Hα. The early-time spectra also show a forest of Fe II lines and the Ca II NIR triplet lines with P Cygni profiles. The initial blue light-curve peak with a red plateau together with weakening Hα with time and NIR excess suggest that ZTF21 acpkzcc is an LRN. The high luminosity of ZTF 21acpkzcc is similar to the LRN AT 2017jfs (Pastorello et al. 2019b), suggesting a massive binary origin.

We note that two additional LRNe were reported in the last three years: AT 2018bwo (Blagorodnova et al. 2021) and AT 2020kog (Pastorello et al. 2021b). AT 2020kog was missed by ZTF because it landed in the chip gaps of the ZTF detector. AT 2018bwo was discovered on 2018 May 22, when ZTF was in the reference-building phase. The first ZTF visit to the field of AT 208bwo was two months later on 2018 July 14. No alerts were generated, as this field did not have a ZTF reference image. We ran post facto image subtractions and measured forced PSF photometry, recovering two detections of AT 2018bwo in the r band at 19.76 ± 0.08 and 20.15 ±0.12 mag on 2018 July 21 and 2018 July 24, respectively.

2.2.3. LRN-silver

This category includes two sources that do not show all the hallmarks of an LRN but do resemble LRNe in several aspects. Their light curves are plotted in Figure 1, and their optical and NIR spectra are shown in Figures 2 and 3, respectively.

1. ZTF 18abwxrhi (AT 2018gzz) has a peak $M_r = -14.82 \pm 0.17$ mag and shows two pronounced light-curve features: a blue first peak followed by a longer-lasting red peak/plateau. Our photometric data are sparse for the red peak/plateau, as the transient did not brighten significantly above the ZTF sensitivity limits. However, the light-curve evolution inferred from the available data is strikingly similar to that of the LRNe in the gold sample. Additionally, a spectrum taken during the first blue peak shows narrow, marginally resolved Balmer emission lines with $v_{\rm FWHM} \approx 300$ km s^{-1} (ruling out a supernova origin), narrow, unresolved Ca II NIR triplet lines with P Cygni profiles, and narrow Ca II H&K absorption lines. We do not detect Na I D in this spectrum, and hence assume negligible host-galaxy extinction. There is no spectroscopic coverage at late times. Given these similarities with LRNe, ZTF 18abwxrhi is most likely an LRN, and we include it in the LRN-silver category.

2. ZTF 21aaekeqd (AT 2021afy) is located on the outskirts of the galaxy UGC 10043. While Pastorello et al. (2022) classify this transient as an LRN, their late-time spectra do not show obvious molecular absorption features (e.g., like those seen in ZTF 21aancgbm). We also do not identify similar molecular features in any of our spectra. As noted by Pastorello et al. (2022), the light curve differs from that of other LRNe with similar luminosities. For these reasons, we include ZTF 21aaekeqd in our LRN-silver sample. It is possible that obvious molecular features appear at later times, where spectroscopic coverage does not exist.

The transient has a 100 day light curve with two low-contrast peaks and is detected only in the r and i bands by ZTF. In our earliest spectrum, we detect Na I D absorption with equivalent width 1.8 ± 0.6 Å, consistent with Pastorello et al. (2022). This corresponds to $E(B-V)_{\rm host} \approx 0.28 \pm 0.10$ mag, assuming that the interstellar medium alone is responsible for the Na I D absorption. However, we caution that this is unlikely, given the remote location of the transient in the host. It is possible that the sodium absorption originates in circumstellar dust around the progenitor of the explosion, in which case the extinction estimate will be incorrect (Poznanski et al. 2012). Accounting for the Galactic component, we adopt a total $E(B-V) = 0.33 \pm 0.10$ mag. With this, the transient reaches $M_{r,\rm peak} = -13.95 \pm 0.16$ mag, and is one of the more luminous members of our sample. We obtained an epoch of J-band imaging at +60 days since peak brightness with $J - r \approx 1$ mag, similar to other LRNe.

Our spectroscopic coverage comprises three optical spectra at phases of +33 days, +89 days, and +114 days, and one NIR spectrum at +92 days since first peak. The +33 day spectrum shows a reddened continuum with narrow Hα ($v_{\rm FWHM} \approx 650$ km s^{-1}) and the Ca II NIR triplet in absorption. Of the three Ca II triplet lines, we detect only the 8542 Å and 8662 Å absorption lines. This is likely because the transition probability for the 8498 Å line is a factor of ∼10 smaller than for the other two. Notably, the absorption lines are unresolved, with $v_{\rm FWHM} \leqslant 200$ km s^{-1} (the instrumental resolution in this wavelength range is $v_{\rm inst} \approx 250$ km s^{-1}, measured from night-sky emission lines). This velocity is much lower than the Hα photospheric velocity at this phase (∼650 km s^{-1}). These absorption lines likely originate in a dense, slow-moving shell of CSM outside the photosphere that was likely ejected prior to the explosion, possibly during the CE phase. The +89 day spectrum shows a more reddened continuum with slower, marginally resolved Hα ($v_{\rm FWHM} \approx 400$ km s^{-1}) and narrow Hβ ($v_{\rm FWHM} \approx 300$ km s^{-1}). The Ca II NIR triplet lines are now seen as a superposition of an emission component with $v \approx 500$ km s^{-1}, and a central narrow absorption component (see Figure 5). A possible explanation for this is that the ejecta have crashed into the CSM at this epoch, and the resulting shock has swept up only part of the CSM. A photosphere forms at the shock interface from which the emission lines originate (Ca II predominantly excited by collisions). The narrow, weak absorption component originates from the unshocked CSM shell lying outside the photosphere. The +80 day NIR spectrum shows similar narrow hydrogen emission lines. The spectrum also exhibits a weak, broad feature in the H band, which is similar to the H_2O absorption seen in ZTF 21aagppzg.

The final optical spectrum at +113 days shows a very weak continuum, but extraordinarily strong Hα ($v_{\rm FWHM} \approx$ 300 km s^{-1}) and strong, unresolved Hβ ($v_{\rm FWHM} < 400$ km s^{-1}). The Ca II NIR triplet is seen purely in emission. This suggests that the shock has swept up all the CSM. The Balmer decrement in this spectrum is $\beta \approx 7$, supporting the notion that the emission originates in an interaction-dominated region. The absorption to emission transition of the Ca II line profiles suggests that there is a dense, slow-moving shell of CSM around the progenitor. None of the other LRNe in our sample undergo such a transition. The late-time spectrum with very strong emission lines is unlike the late-time optical spectra of

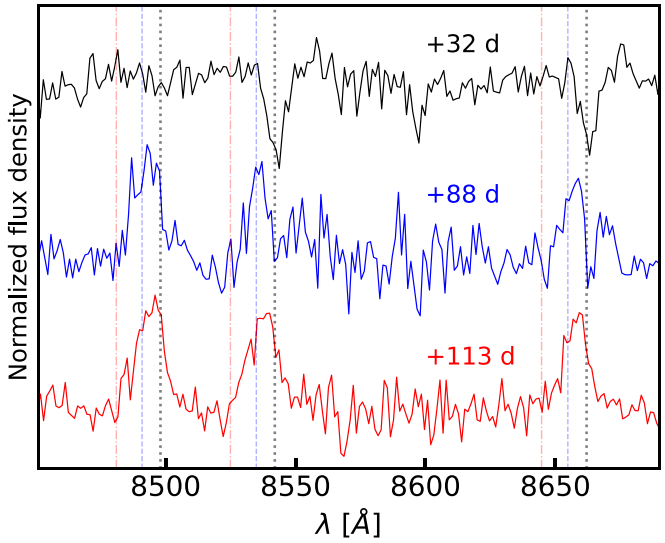

Figure 5. Evolution of Ca II line profiles of ZTF 21aaekeqd. In the earliest spectrum (+32 days, black), the lines are seen purely in absorption and likely originate from a shell of slow-moving CSM around the binary. In the second spectrum, the profile has transitioned to emission with a narrow absorption component. This is likely because the ejecta have crashed into the CSM and swept up only part of the CSM. The shocks in the ejecta produce the emission, while the absorption comes from the unshocked, dense CSM shell outside the photosphere. In the final optical spectrum, the line profiles are pure emission, suggesting that all of the CSM has been swept up by the ejecta.

other LRNe in our sample (e.g., ZTF 21aancgbm at 360 days) that show strong molecular absorption bands.

2.2.4. LRN-bronze

This category includes three sources (ZTF 18aajqkmr, ZTF 20abjgdec, and ZTF 21aabfwwl) that show multiple peaks in their light curves but do not have spectroscopic coverage (see Figure 1). These transients have peak absolute magnitudes of −15.36, −14.37, and −15.72 mag, respectively. ZTF 21aabfwwl was initially classified as a Type II SN (Hinkle 2021), but the spectrum available on TNS is noisy and no H lines are clearly visible. We list these three transients as candidate LRNe.

2.2.5. ILRT-gold

This category includes six sources that we spectroscopically classify as ILRTs. Their light curves are shown in Figure 6. We calculate the distances and extinction due to the Milky Way as was done for the LRNe (see Section 2.2.2). It is challenging to estimate the host-galaxy extinctions because ILRTs have extremely dusty progenitors and often exhibit variable Na I D originating in outflows (Smith et al. 2009; Cai et al. 2021; also see discussion of ZTF 19acoaiub below). Instead, we use the peak optical $g-r$ colors of ILRTs to estimate the host-galaxy extinction, similarly to Humphreys et al. (2011), Smith et al. (2009), and Jencson et al. (2019). The spectra of ILRTs at peak brightness show F-type absorption features, suggesting $T\approx 7500$ K. Cai et al. (2021) find that the ILRTs in their sample have peak $B-V$ colors in the range 0.2–0.4 mag, consistent with this interpretation. We use the peak colors of the ILRTs in our sample to estimate the value of $E(B-V)_{\rm host}$ required to bring the colors into this range. We estimate a non-negligible extinction for two ILRTs in our sample—$E(B-V)\approx 0.7$ mag for ZTF 19aadyppr (consistent with Jencson et al. 2019) and $E(B-V)\approx 0.2$ mag for ZTF 19aagqkrq. For the other transients, we assume the extinction to be dominated by the Galactic component. We calculate pseudobolometric luminosities by fitting blackbodies to the available data. Table 3 lists the derived photometric properties of the ILRTs. Our optical and NIR spectra of these transients are shown in Figures 7 and 8, respectively. Similarly to the case of the LRNe, here we derive line velocities by fitting Lorentzian profiles and list the derived values in Table 4. We briefly discuss the properties of the transients here.

Two of these transients (ZTF 19aadyppr and ZTF 21aclzzex) have spectroscopic coverage extending to late times. Of these, ZTF 19aadyppr is in the galaxy M 51 and has been studied in detail by Jencson et al. (2019), who identified its red, dusty progenitor. The object shows a single-peaked red light curve, and its spectra exhibit narrow Hα and [Ca II] emission, characteristic of ILRTs.

ZTF 21aclzzex is the brightest ILRT in our sample, with peak $M_r=-15.68\pm0.16$ mag. Our light-curve coverage is sparse and noisy, but the available data show indications that the transient is red and possibly has multiple peaks. However, our spectroscopic coverage extends to 163 days since peak and resembles the evolution of ILRTs. An early-time spectrum at 9 days since peak brightness shows a blue continuum with narrow Hα, Hβ, Ca II, and [Ca II] emission. The spectrum also has Ca II H&K absorption. The next optical spectrum obtained at 84 days since peak shows a reddened continuum with narrow Hα, Ca II, and [Ca II] emission, as well as Ca II H&K absorption. [O I] is detected as a weak emission line. The 118 day optical spectrum displays similar features, except [O I] has become stronger. Similar [O I] emission was observed in the ILRT AT 2013la (Cai et al. 2021). The 134 day NIR spectrum shows strong, narrow hydrogen emission lines, as well as He I and O I emission. Although the light curve is not informative enough to classify the transient, the spectroscopic evolution is strikingly similar to that of several ILRTs, especially with [Ca II] emission seen consistently in all spectra. For this reason, we classify it as an ILRT.

The other four transients have only early-time spectroscopic coverage. Analogous to the other ILRTs, they all exhibit narrow Hα and [Ca II] emission in their spectra. We note that, while the LRN AT 2018hso also showed [Ca II] emission in its early spectra, it also had two pronounced peaks in its light curve. None of these four transients show multiple peaks, and they are not AT 2018hso-like LRNe. We thus classify them as ILRTs based on narrow Hα and [Ca II] emission and the lack of multipeaked light curves.

Of these four, ZTF 19acoaiub (AT 2019udc) and ZTF 19aagqkrq (AT 2019ahd) have the best-sampled light curves. ZTF 19acoaiub is located in NGC 718 and has peak $M_r=-14.68\pm0.04$ mag and a relatively fast-declining, single-peaked light curve. The ZTF light curve also samples the pre-peak rise. Seven days before peak, the transient was extremely red, with $g-r\approx0.8$ mag. As it brightens, the transient also evolves to bluer colors of $g-r\approx0.4$ mag five days before peak and $g-r\approx0.2$ mag at peak brightness. The transient then declines at a rate of $\sim$0.03 mag day^{-1} for the next 60 days as it evolves back to redder colors. Our only optical spectrum was obtained 7 days before the peak and shows strong Hα emission with $v_{\rm FWHM}\approx1300$ km s^{-1}. This spectrum also displays narrow Ca II and [Ca II] emission, similarly to several other ILRTs. This pre-peak spectrum shows very strong Na I D absorption with EW $\approx 4.8\pm0.7$ Å consistent with its

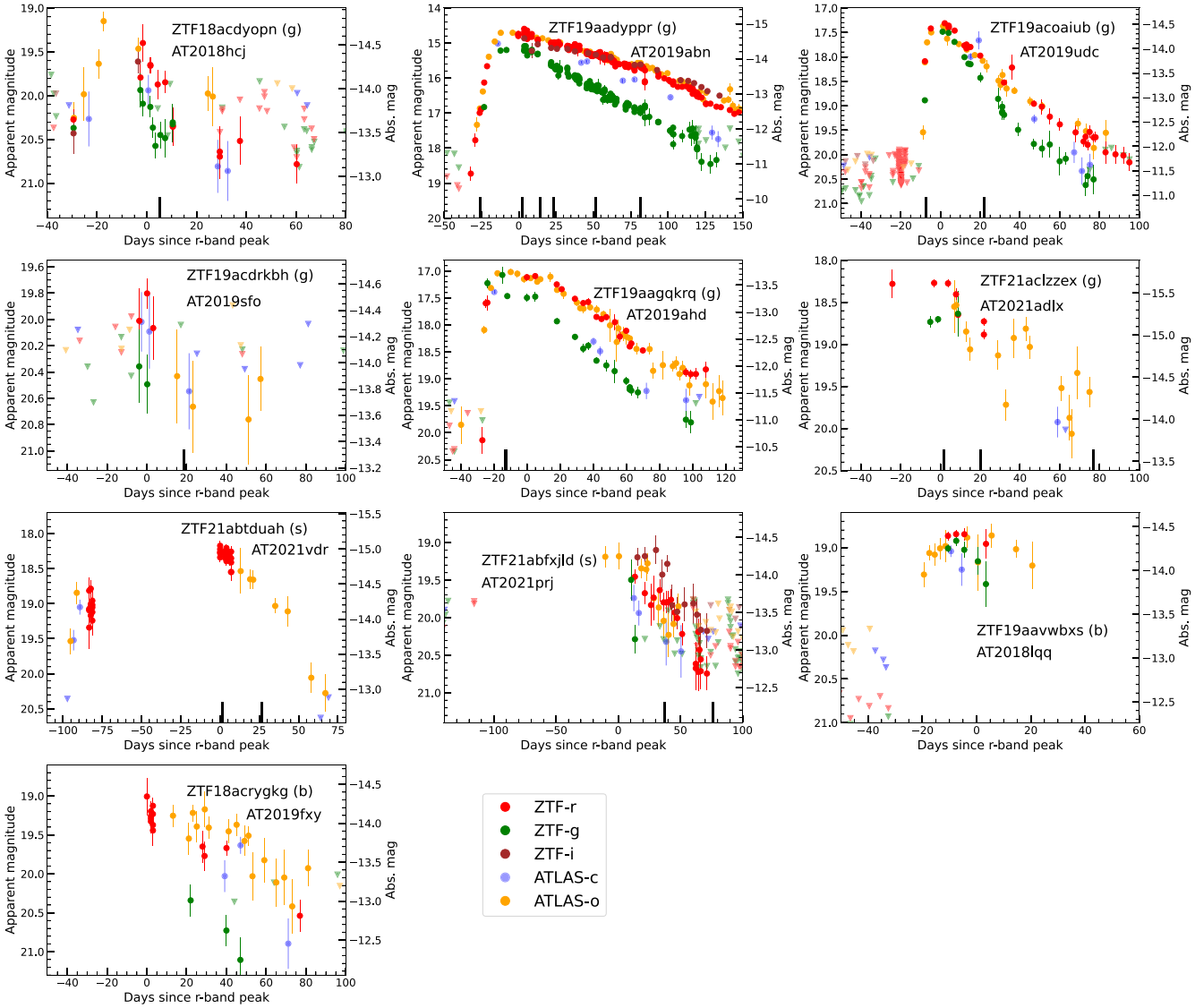

Figure 6. Forced-photometry light curves of the 10 ILRTs in our sample. The transients in the gold, silver, and bronze samples are marked in parentheses with "*g*," "*s*," and "*b*" (respectively). The ZTF-*g*, ZTF-*r*, ZTF-*i*, ATLAS-*c*, and ATLAS-*o* data points are plotted in green, red, brown, blue, and orange circles (respectively). Downward-pointing triangles indicate 5σ upper limits. The days are in the observer frame. The light curves have been corrected for extinction using the values listed in Table 3. Solid black vertical lines indicate epochs at which spectra were obtained.

pre-peak red colors. A likely explanation for this behavior is that the progenitor of ZTF 19acoaiub was dust-enshrouded. The circumstellar dust was destroyed by the explosion, causing the transient to evolve to bluer colors as it brightened. This transient demonstrates the issue with using early-time Na I D features to estimate the host-galaxy extinction.

ZTF 19aagqkrq (AT 2019ahd) has peak $M_r = -13.72 \pm 0.15$ mag and a blue color up to a few days before peak, but rapidly transitions to red colors. Our spectroscopic coverage comprises two optical spectra obtained on successive nights at peak brightness and 1 day post peak. Both spectra show Hα emission with $v_{\rm FWHM} \approx 700$ km s^{-1} and strong Ca II and [Ca II] emission lines.

The remaining two—ZTF 18acdyopn and ZTF 19acdrkbh—have relatively sparse light-curve sampling. ZTF 18acdyopn has a peak absolute magnitude $M_r = -14.33 \pm 0.19$ mag and declines by 1.5 mag in the *r* band in 80 days. Although our light curve does not sample the peak, the available data show that the transient had red colors a few days post peak. An optical spectrum taken five days since peak shows narrow hydrogen Balmer emission lines ($v_{\rm FWHM} \approx 300$ km s^{-1}), [Ca II], Ca II H&K, as well as Ca II NIR triplet emission lines. Similarly, ZTF 19acdrkbh has peak $M_r = -14.62 \pm 0.15$ mag, was detected at the threshold of ZTF sensitivity, and has $g - r \approx 0.6$ mag at peak. An optical spectrum at +19 days since peak shows narrow Hα ($v_{\rm FWHM} \approx 600$ km s^{-1}) emission and possible Na I D absorption, similarly to other ILRTs.

2.2.6. ILRT-silver

This category includes two sources (ZTF 21abtduah and ZTF 21abfxjld) that show luminosities and spectral evolution broadly similar to ILRTs, but do not have [Ca II] emission. Although [Ca II] emission in ILRTs is a sign of interaction with the surrounding CSM, its strength is sensitive to the CSM density (Humphreys et al. 2011). For example, the proposed ILRT AT 2019krl did not exhibit Ca II emission in several of its spectra (Andrews et al. 2021).

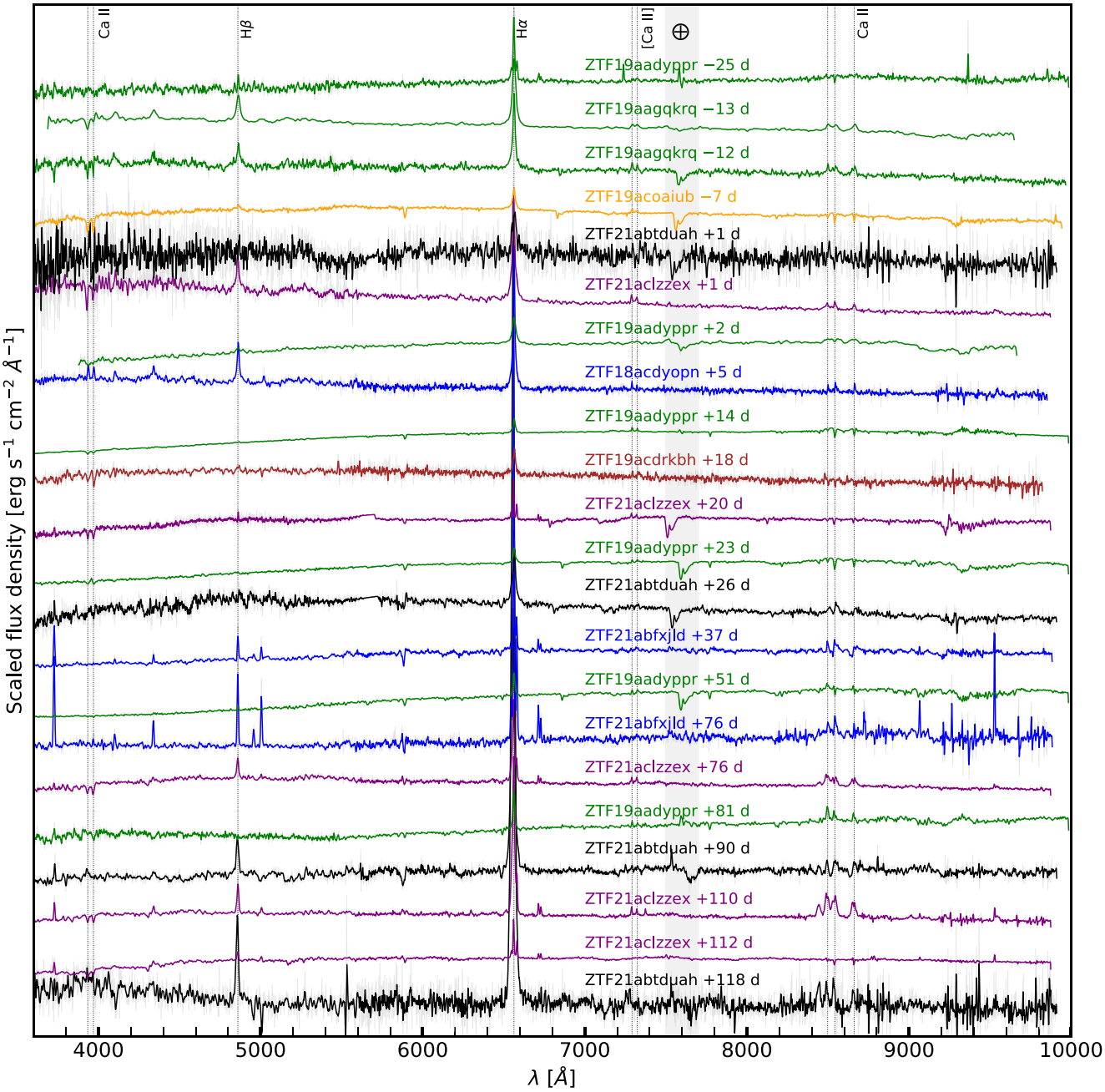

Figure 7. Optical spectra of ILRTs presented in this paper.

For both transients, our light-curve coverage does not sample the peak, and it is unclear whether they have multiple peaks. For ZTF 21abtduah, our light curve samples the brightening and fading of the transient (see Figure 6). We estimate a fiducial peak time by fitting a polynomial to these points. For ZTF 21abfxjld, the ZTF light curve samples the fading of the object. However, the ATLAS *o*-band light curve shows two measurements separated by 5 days that do not demonstrate significant evolution, suggesting that the transient peaked around then. We determine the peak time by fitting a polynomial to the ATLAS *o*-band light curve. We have late-time spectroscopic coverage of both these transients. In a spectrum taken 24 days since the (fiducial) peak, ZTF 21abtduah shows Hα with $v_{\rm FWHM} \approx 1200$ km s^{-1}. A second spectrum obtained at 48 days since peak shows a double-peaked Hα profile, suggesting interaction with slow-moving CSM, or absorption in an external shell. This spectrum also shows the narrow Ca II NIR triplet in emission. The final spectrum taken at 140 days since peak displays strong Hα, Hβ, Ca II NIR, and O I emission lines, similar to those of ZTF 21aclzzex and AT 2013la (however, [Ca II] lines are not seen). The Hα profile in this spectrum is also double-peaked. ZTF 21abfxjld has spectra at 44 days and 83 days since peak, both of which show Hα emission with $v_{\rm FWHM} \leqslant 300$ km s^{-1}, and narrow [Ca II] emission. We also have two NIR spectra taken at 26 days and +125 days since peak. The +26 days NIR spectrum has narrow H emission lines. However, the +125 days spectrum shows strong but narrow H and He absorption in the *J* band. Such features are not seen in any other ILRTs.

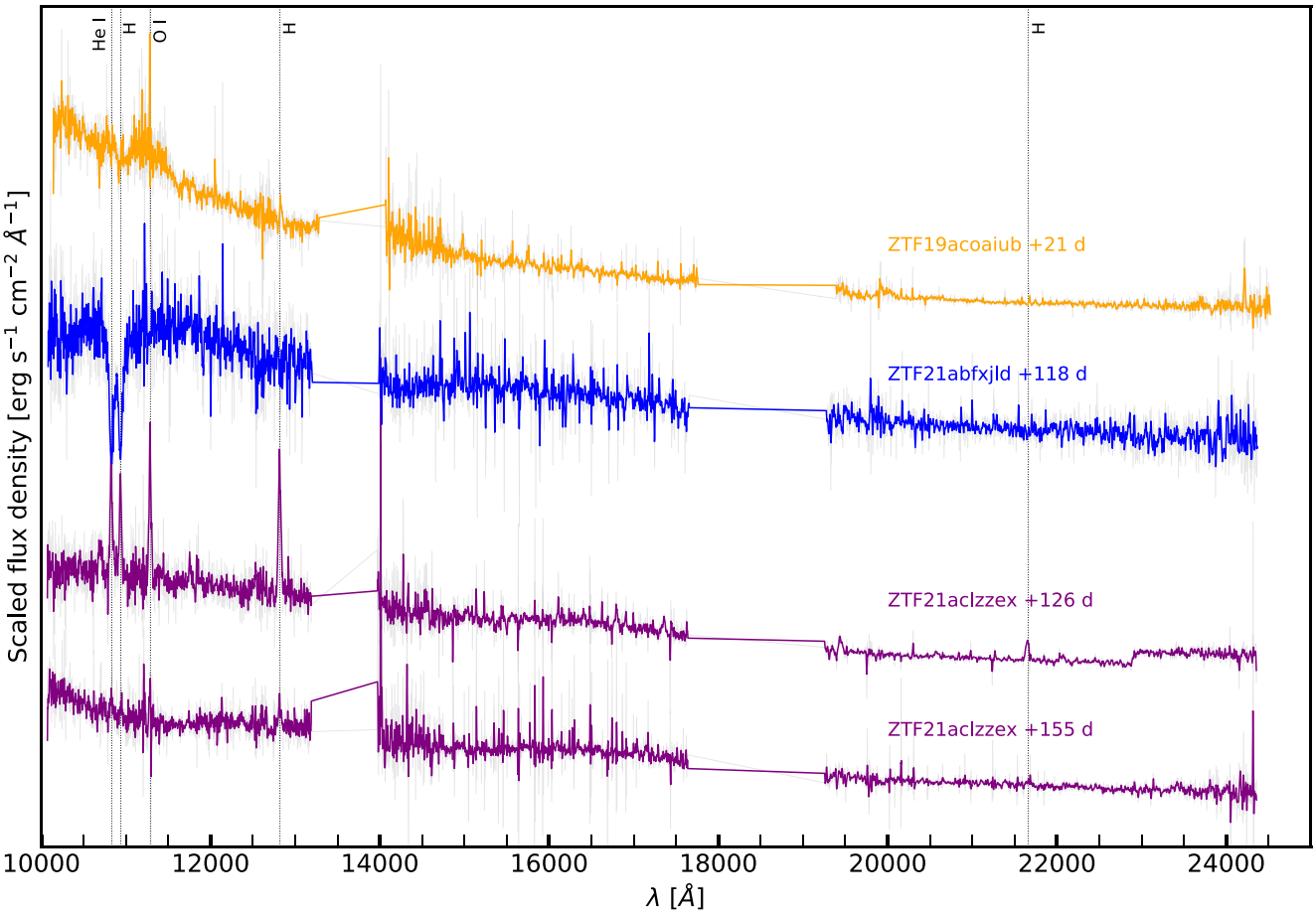

Figure 8. NIR spectra of ILRTs presented in this paper.

The low expansion velocities of these transients argue against a core-collapse SN origin for them. The lack of any molecular features at late times rules out LRNe. None of them show any significant outbursts in archival data. The nature of these transients is not completely clear. Their spectral features point toward CSM interaction. The lack of Ca II emission suggests that the CSM is denser than in typical ILRTs. These transients could represent a peculiar variety of ILRTs. For these reasons, we classify these as ILRT-silver sources.

2.2.7. ILRT-bronze

This category includes two sources: ZTF 19aavwxbs and ZTF 18acrygkg. ZTF 19aavwxbs shows a single peak lasting 20 days in the ZTF and ATLAS light curve before it went into solar conjunction. A low-resolution ($R \approx 100$) spectrum of ZTF 19aavwxbs taken with the Spectral Energy Distribution Machine (SEDM; Blagorodnova et al. 2018; Rigault et al. 2019) spectrograph on the 60 inch telescope at Palomar Observatory shows Hα emission with $v_{\rm FWHM} \leqslant 3000$ km s^{-1}. No other features are discernible in the spectrum. ZTF 18acrygkg has a light curve lasting for 40 days in the ZTF data. There is no spectroscopic data for ZTF 18acrygkg. It is possible that both of these transients are low-luminosity Type II SNe, so we only list them as ILRT candidates.

2.2.8. Ambiguous Sources

Finally, we have seven sources with no spectroscopic coverage and for which the photometric data are insufficient to determine a tentative classification. Most of these sources are likely SNe where the ZTF data sample the late-time phases. The 5σ alert light curves of these transients have durations shorter than 25 days.

3. Volumetric Rate

To estimate the volumetric rates, we simulate the ZTF survey from 2018 June 1 to 2022 February 20 with the Python package `simsurvey` (Feindt et al. 2019) using the ZTF pointing history and actual ZTF difference images to estimate the limiting magnitudes of each pointing. Using template light curves, we then inject LRNe and ILRTs for a range of possible rates and identify the number of transients that would be detected by the selection criteria of our experiment. Comparing simulations to the observed LRN/ILRT sample gives a first estimate of the rate. This estimate is then corrected for selection effects such as the spectroscopic completeness of the CLU experiment and the CLU galaxy catalog.

3.1. Template Light Curves

LRNe exhibit a dichotomy in their light curves. The brighter LRNe ($M_r \geq -11$ mag) are characterized by a double-peaked

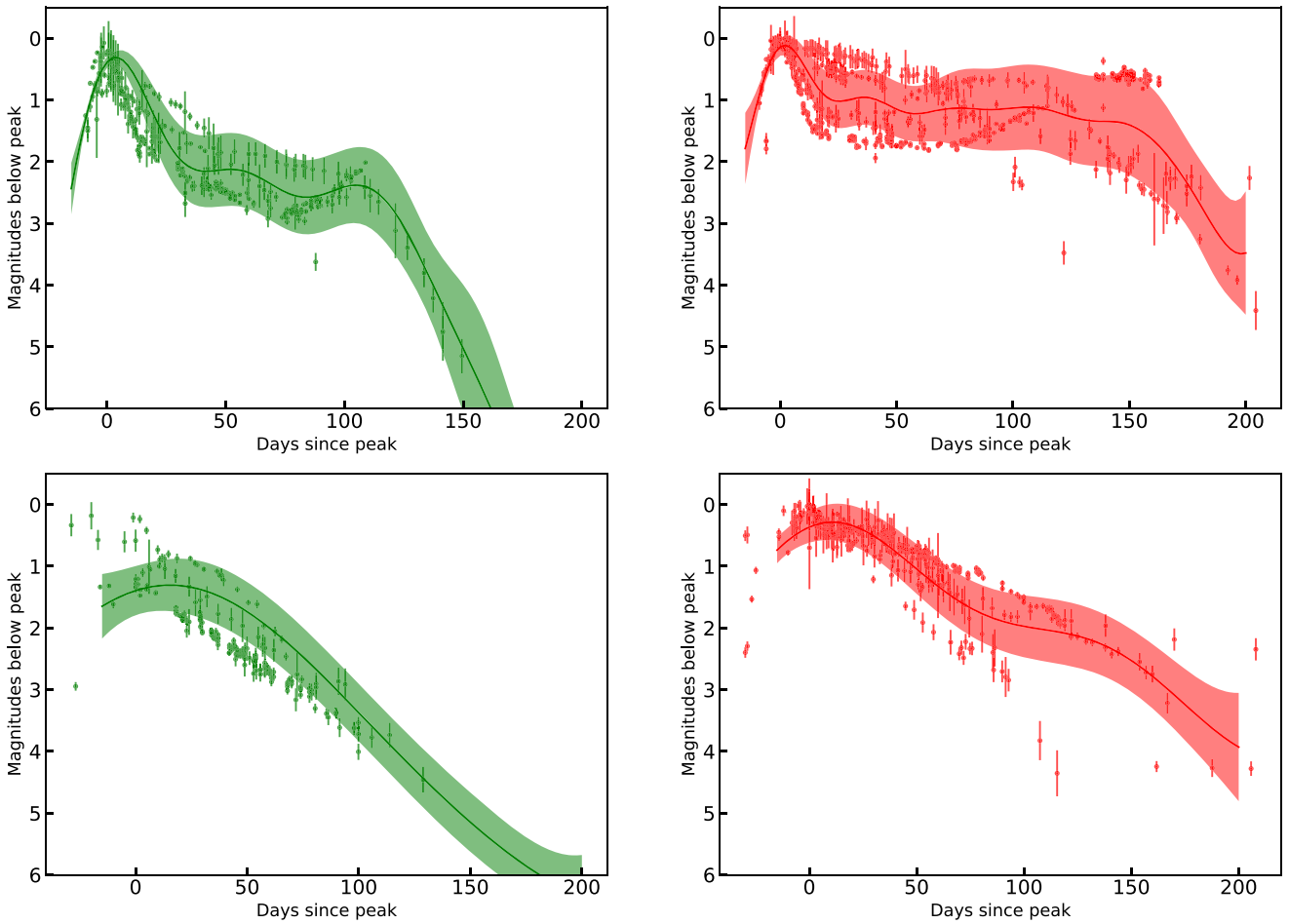

Figure 9. Light-curve templates in g and r (green and red colors, respectively) for LRNe (top row) and ILRTs (bottom row). The solid points depict light curves of transients that were used to build the templates. The line and shaded regions show the templates and 68% uncertainties derived from Gaussian process fits to the transients. The templates capture the essence of the photometric evolution of LRNe (initial blue peak + long-lived second peak/plateau) and ILRTs (single peak, red light curve). These templates are available online (see Section 7).

light curve, while the lower-luminosity events have a single peak and much shorter durations (Pastorello et al. 2019a; Blagorodnova et al. 2021). All except one of the ZTF events are brighter than −11 mag and have double-peaked light curves lasting for ∼150 days. ZTF 19adakuot, with $M_{\rm r,peak} \approx -9.5$ mag, is the least luminous event in our sample and fades quicker than any of the other events. Owing to the different light-curve shapes and durations of the brighter LRNe and the fact that most of the ZTF LRNe belong to this category, we restrict our rate analysis to events with $M_{\rm r}$ brighter than −11 mag.

We created an empirical LRN light-curve template using the three well-sampled LRNe in our sample with $M_{\rm r,peak} \leqslant -11$ mag and two double-peaked LRNe from the literature, AT 2017jfs (Pastorello et al. 2019b) and AT 2020kog (Pastorello et al. 2021b). We first normalized the g- and r-band light curves by their peak magnitude in the respective filter. We then fit a Gaussian Process model with a radial basis function (RBF) kernel to the normalized light curve. The g- and r-template light curves of the LRNe are shown in the top row of Figure 9 and provided online.

The light curves of ILRTs are more homogeneous than those of LRNe. We construct light-curve templates using g-band light curves of four ILRTs (AT 2018aes, AT 2019abn, AT 2019udc, and AT 2019ahd) and r-band light curves of these and four additional ILRTs (AT 2010dn, AT 2012jc, AT 2013la, and AT 2013lb). The ILRT templates are shown in the bottom row of Figure 9. Both LRN and ILRT template light curves are available online (Section 7).

3.2. Luminosity Function

In this paper, we have presented the first controlled sample of LRNe and ILRTs from a systematic survey. We use this sample to calculate the luminosity function of LRNe and ILRTs.

We restrict ourselves to all gold and silver LRNe that have peak absolute magnitudes brighter than −11. Figure 10 shows a histogram of the peak absolute magnitudes of the events in the ZTF sample. As the events are detectable out to different volumes (all smaller than the CLU volume limit of 200 Mpc), the histogram needs to be volume corrected to determine an accurate luminosity function. The volume-corrected distribution of peak absolute magnitudes of LRNe in our sample is plotted in Figure 10 with a different color. Each event has been weighted by $1/V_{\rm max}$, where $V_{\rm max}$ is the maximum volume out to which that event can be detected ($V_{\rm max} \propto 10^{\frac{3}{5}(20-M_{r,\rm peak})}$). The volume-corrected distribution shows a steep decline of the event rate with increasing peak luminosity. Figure 10 also shows the distribution of the ZTF events combined with events

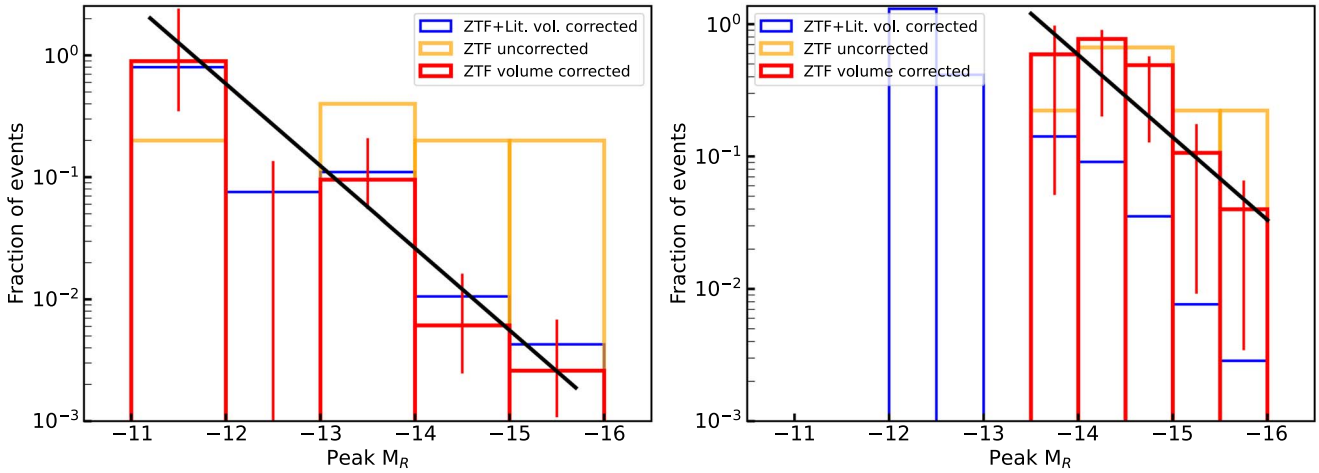

Figure 10. Distribution of the peak absolute magnitudes of LRNe (left) and ILRTs (right) in our sample. The volume-corrected ZTF sample with Poisson error bars is shown in red, and the volume-corrected ZTF+literature sample is shown in blue. The black line illustrates a linear fit to these data (in log space). We derive a luminosity scaling $dN/dL \propto L^{-2.5\pm0.3}$ for LRNe and $dN/dL \propto L^{-2.5\pm0.5}$ for ILRTs.

from the literature (taken from Blagorodnova et al. 2021). The distribution of the ZTF events is broadly consistent with that of the ZTF+literature events (although there are significant biases associated with the literature sample). The peak-luminosity distribution of ZTF events is fit well by a straight line (in log space) with slope 0.6 ± 0.1. This corresponds to $dN/dL \propto L^{-2.5\pm0.3}$, significantly steeper than the luminosity function derived for low-luminosity ($M_V > -10$ mag) LRNe (Kochanek et al. 2014). The implications of these differences are discussed in Section 4.1.

Similarly, we calculate the ILRT luminosity function using the eight gold and silver events from our sample. Figure 10 (right panel) shows the volume-corrected distribution of the peak absolute magnitudes of ZTF ILRTs. We fit a straight line with slope 0.6 ± 0.2 to the distribution (in log space), for $M_r < -13.5$ mag. This corresponds to a luminosity function of $dN/dL \propto L^{-2.5\pm0.5}$. This scaling only samples the brighter end of the ILRT luminosity function. Figure 10 also shows the distribution of previously known events from literature together with the ZTF sample, which extends to lower luminosities than the ZTF sample ($M_r \approx -12$ mag). We note that, for both LRNe and ILRTs, including the bronze or excluding the silver sample does not significantly change the derived luminosity function.

3.3. Subsample for Rate Estimates

As mentioned in Section 2.2, only 19 of the 34 transients in Table 1 have spectra. The low spectroscopic completeness of this sample compared to the full CLU experiment is because it includes several transients with sparse photometric coverage (Section 2.2.8). These transients either entered solar conjunction soon after discovery or were discovered after they emerged from solar conjunction and faded away before any spectra were obtained. To exclude such transients from the sample, we introduce an additional selection criterion—a minimum threshold of 25 days on the duration of the ZTF light curve (i.e., the 5σ detections in g or r should span at least 25 days). Of the 21 sources that satisfy this criterion, 16 have spectra giving a spectroscopic completeness of ∼80% for the sample—consistent with that of the full CLU experiment.

We then build a subsample from these 21 candidates to use for LRN/ILRT rate calculations. All sources listed as potential LBVs are naturally excluded, and all "ambiguous" sources are excluded by the light-curve-duration criterion. Of the remaining sources, we only include those transients that have spectroscopic coverage (i.e., the gold and silver categories) to obtain an estimate of the rate, as this estimate is subsequently corrected for spectroscopic completeness. The subsample used for rate calculations is marked with an asterisk in Table 1.

The LRN subsample used for rate estimates comprises seven out of the eight gold and silver LRNe from Table 1. ZTF 19adakuot is excluded because of its low luminosity (Section 3.2). As noted in Section 2.2.2, the LRNe AT 2018bwo and AT 2020kog were not detected in the ZTF alert stream. Two detections of AT 2018bwo were recovered post facto, but this object is excluded by the light-curve-duration criterion. AT 2020kog is excluded because it was in the chip gaps of the ZTF camera, an effect that is taken into account by our survey simulations. The ILRT subsample comprises five out of the eight gold and silver ILRTs. The remaining three do not satisfy the light-curve-duration criterion.

3.4. Volumetric Rates

The luminosity functions and template light curves were used to simulate LRNe and ILRTs, and the `simsurvey` simulations of the ZTF survey were used to count how many of them would be detected by our experiment. We apply the selection criteria described in Section 2.1 and the light-curve-duration criterion from Section 3.3 to the simulated transients. We conduct 100 iterations of simulations for each rate to estimate the median and 1σ uncertainties on the number of transients recovered for each rate.

The top left panel of Figure 11 shows the number of LRNe that would be detected by our selection criteria as a function of their volumetric rate. The top right panel of Figure 11 gives a histogram of the fraction of simulations where the number of detected simulated transients equals the observed number of seven LRN-gold and LRN-silver events. We fit the distribution with a skewed Gaussian function to estimate the median and 68 percentile confidence limits. Accounting for an additional Poisson uncertainty associated with the seven observed events, we derive a volumetric rate of $r_{\mathrm{LRN},u} = 5.7^{+4.4}_{-2.7} \times 10^{-5}$ Mpc^{-3} yr^{-1}.

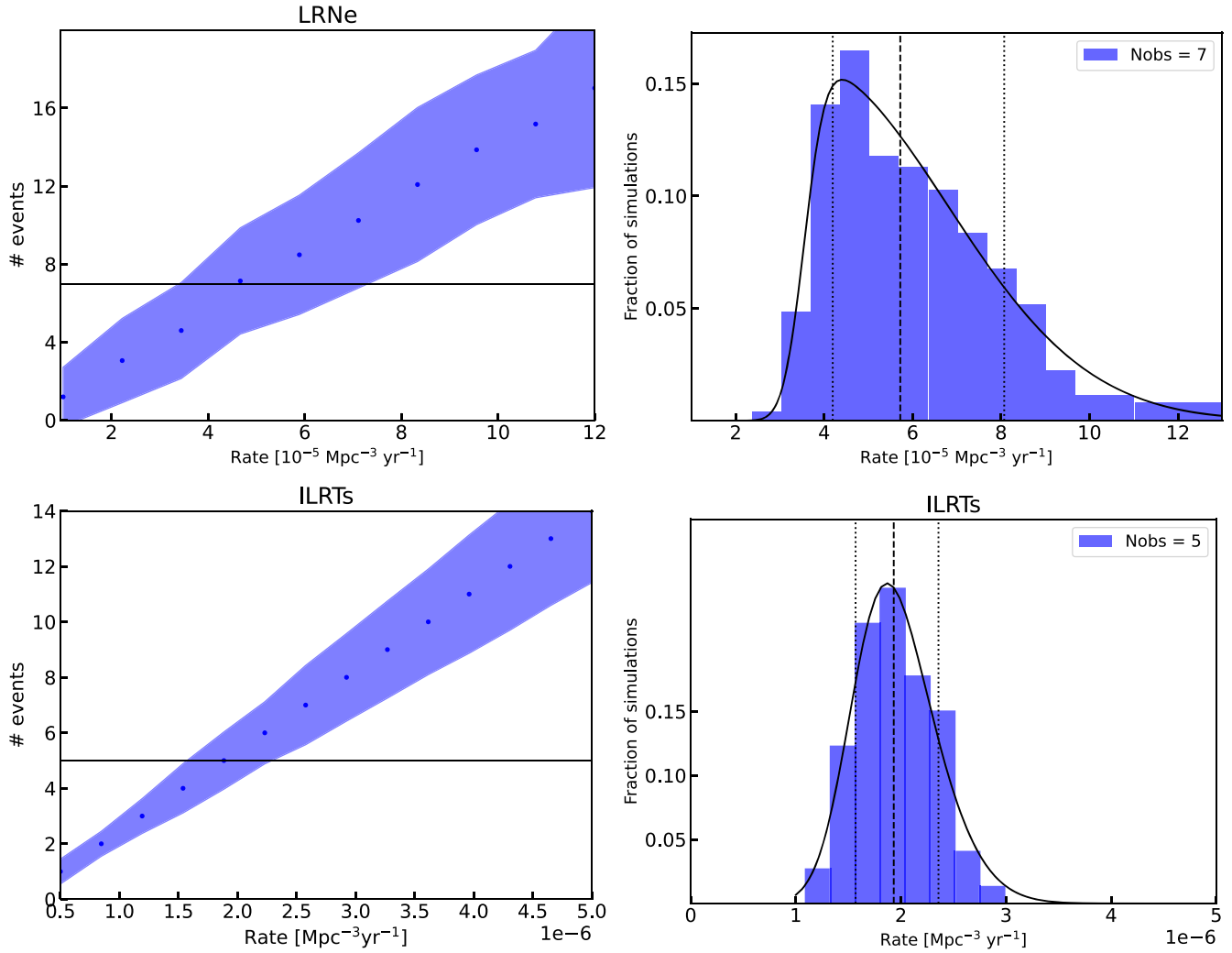

Figure 11. Left: the number of simulated LRNe (top) and ILRTs (bottom) that pass our filtering criteria as a function of their volumetric rate. Right: the fraction of simulations where the number of simulated transients that pass the filtering criteria equals the observed number of LRNe (top) or ILRTs (bottom). The distributions are fit by a skewed Gaussian function, indicated as black solid curves. The vertical dashed and dotted lines show the median and 68th percentile confidence limits of the distribution, respectively.

This estimate does not account for four factors that may result in underestimation compared to the true LRN rate: (1) the CLU experiment is limited to 100″ or 30 kpc from nuclei of galaxies and will miss farther transients, (2) the CLU experiment is not 100% spectroscopically complete, (3) the CLU experiment relies on the CLU galaxy catalog and is affected by its completeness, and (4) some LRNe will be missed due to inefficiencies of the ZTF image-subtraction pipeline. First, we note that all literature events have been discovered within 100″ or 30 kpc of their respective hosts. We searched through transients classified as part of the ZTF BTS—an all-sky, magnitude-limited survey with ZTF—and did not find any additional LRNe. For this reason, we believe that the CLU offset criterion does not have a significant effect on the rate estimate. Second, the CLU experiment is ∼80% spectroscopically complete for $mr < 20$ mag transients. This suggests that the completeness-corrected rate is $7.1^{+5.9}_{-3.4} \times 10^{-5}$ Mpc^{-3} yr^{-1}. However, the CLU completeness is a function of apparent magnitude, and varies from 100% for $mr < 18$ mag to 95% for $mr < 19$ mag. To account for this, we calculate the completeness as a function of apparent magnitude in bins of 1 mag. For each simulation of each of our rates, we bin the simulated transients by peak apparent magnitude and count only the fraction of events that would be classified based on the CLU criteria. This exercise gives a value consistent with the simplified approach described above, because a majority of the events have faint apparent magnitudes and the (large) uncertainties on this estimate are dominated by small-number statistics.

Third, to correct for the incompleteness of the galaxy catalog, we used the redshift completeness factor (RCF) derived from the BTS. As all events in our sample come from star-forming galaxies, we calculate the RCF for star-forming galaxies in the BTS sample as a function of redshift (z) and WISE 3.36 μm absolute magnitude ($M_{\rm W1}$) as described by Fremling et al. (2020). We then use the redshifts and $M_{\rm W1}$ magnitudes of the host galaxies of LRNe in our sample and weight each event by $1/{\rm RCF}(z, M_{W1})$ to estimate the effect of galaxy-catalog incompleteness. We find that this leads to an underestimation of the rate by ∼10%.

Finally, the ZTF image-subtraction pipeline has two possible sources of inefficiency that are relevant for this calculation. In each science image, the pipeline actively masks pixels that are affected by quality cuts (e.g., saturation owing to high

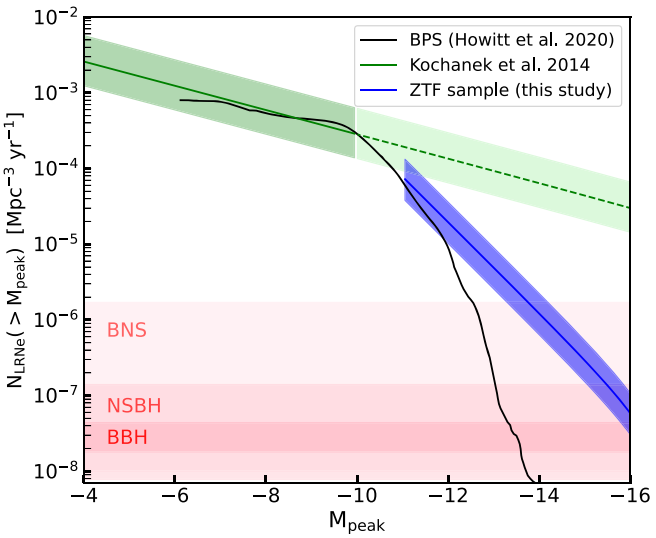

Figure 12. The rate of LRNe brighter than a given absolute magnitude as determined from our ZTF sample (blue), the Galactic sample of Kochanek et al. (2014) sample (green), and the binary population synthesis models of Howitt et al. (2020) (black line). The Kochanek et al. (2014) sample was restricted to $-10 \leqslant M_V \leqslant -4$ mag, while the ZTF sample is restricted to $-16 \leqslant M_r \leqslant -11$ mag. The green dashed line indicates the Galactic rate extrapolation to brighter luminosities. It is evident that the Galactic scaling overpredicts the observed ZTF rate by several orders of magnitude. The steeper drop of the LRN rate at higher luminosities is also seen in the BPS models. The BPS models underpredict the brightest ($M_r \leqslant -13$ mag) rate of LRNe, which could be attributed to specific assumptions about CE physics in the models. The pink shaded regions indicate the constraints on the rates of BNS, NSBH, and BBH mergers as measured by LIGO (The LIGO Scientific Collaboration et al. 2021a). The rates of the brightest LRNe are consistent with a significant fraction of them being progenitors of these compact merging systems.

brightness, cosmic rays, bad pixels). This introduces a time-dependent source of incompleteness. This dynamic masking does not have a significant effect, as LRNe and ILRTs have long durations and are picked up by the pipeline eventually. A more serious issue pertains to the reduced efficiency of the image-subtraction algorithm on bright galaxy backgrounds, as are common for the LRNe and ILRTs in our sample. The ZTF pipeline efficiency as a function of background brightness has not been studied to date, and this analysis is outside the scope of this paper. We therefore caution that our rates are possibly lower limits. Applying the corrections described above (except pipeline efficiency), we derive a corrected rate of $r_{\rm LRNe} = 7.8^{+6.5}_{-3.7} \times 10^{-4}$ Mpc^{-3} yr^{-1} for LRNe.

Similarly, using the ILRT luminosity function and `sim-survey` simulations, we derive an uncorrected rate $r_{\rm ILRT,u} = 1.9^{+1.3}_{-1.0} \times 10^{-6}$ Mpc^{-3} yr^{-1} (see bottom panel of Figure 11). Correcting for the incompleteness effects described above gives $r_{\rm ILRT} = 2.6^{+1.8}_{-1.4} \times 10^{-6}$ Mpc^{-3} yr^{-1}.

4. Discussion

4.1. LRNe

Kochanek et al. (2014) used three Galactic mergers to estimate the rate of low-luminosity stellar mergers with $M_V \geqslant -10$ mag. They find that the luminosity function of these mergers is roughly $dN/dL \propto L^{-1.4\pm0.3}$ and the rate of events brighter than $M_{V,\rm peak} = -3(-10)$ is $\sim$0.5 (0.03)yr^{-1}. Our ZTF sample shows that their scaling does not extend to higher luminosities. For transients brighter than $M_{r,\rm peak} = -11$ mag, the luminosity function drops at a much steeper rate ($dN/dL \propto L^{-2.5}$), suggesting a broken power-law luminosity function for LRNe. Figure 12 shows the LRN rate as a function of peak absolute magnitude derived from our ZTF sample and the Kochanek et al. (2014) scaling. To convert the Galactic rate measurements from Kochanek et al. (2014) to volumetric rates, we follow Howitt et al. (2020) and assume that the LRN rate scales with star formation. We use a star formation rate of 2 $M_\odot$ yr^{-1} for the Milky Way (Licquia & Newman 2015) and an average cosmic star formation rate of 0.015 $M_\odot$ yr^{-1} (Madau & Dickinson 2014). The ZTF and Kochanek et al. (2014) rate estimates diverge at high luminosities. The volumetric rate of LRNe brighter than $M_r = -11$ mag (-13 mag) derived from the ZTF sample is lower by a factor of $\sim$5 (100) than that extrapolated from the Kochanek et al. (2014) scaling.

A steeper luminosity function at the brighter end has also been predicted by binary population synthesis (BPS) models (Howitt et al. 2020). They follow the binary evolution of a population of binary systems with masses drawn from a Kroupa IMF and a binary fraction of unity, and find that 45% of the simulated binaries undergo some form of unstable mass transfer. Of these binaries, 38% result in stellar mergers while the remaining 62% result in CE ejections. Qualitatively similar results were also obtained by the population synthesis study of Politano et al. (2010), although they focused on the remnants of CEE rather than the associated transients. Howitt et al. (2020) used analytical expressions to approximate light curves associated with their simulated mergers and CE ejections, and they determined the Galactic rate of LRNe as a function of their peak luminosity. Figure 12 also shows the volumetric LRN rate from these BPS simulations as a function of peak magnitude. We derive the volumetric rate using the Galactic and average cosmic star formation rates as described above. As noted by Howitt et al. (2020), the BPS rate agrees with the Kochanek et al. (2014) value for low luminosities, but it diverges for $M_{\rm bol} \leqslant -10$ mag. The steep decline in the LRN rate seen in the BPS simulations is consistent with the rates derived from our ZTF sample.

However, we note that the BPS simulations underpredict the rates for LRNe with $M_r < -13$ mag. This could be a result of several assumptions about the LRN light curves, binary populations, or CE physics used in the BPS simulations. Most importantly, Howitt et al. (2020) assumed that the LRN light curve is powered solely by hydrogen recombination and used analytical scaling relations from Ivanova et al. (2013b) to estimate an LRN light curve. But, as noted in their analysis, this model is unable to reach the luminosities of the highest-luminosity LRNe. Similar light-curve modeling by Matsumoto & Metzger (2022) also shows that hydrogen recombination alone cannot explain the light curves of the highest-luminosity LRNe. Additionally, hydrogen recombination is believed to power the plateau in LRNe, and not the initial blue peak (which is used for our rate calculations, as well as those of Kochanek et al. 2014). Using the recombination-powered light-curve model thus underpredicts the LRN rate at the high-luminosity end. More accurate models of LRN light curves are required to reconcile the predicted rate with the observed rate. Several other parameters about binary populations and CE physics can also contribute to the observed discrepancy. For example, a uniform binary fraction was assumed in the simulations, but the binary fraction increases with stellar mass (Moe & Di Stefano 2017). This would mean the number of massive binaries is higher, which would produce additional LRNe at the bright end.

Here, we note that the Kochanek et al. (2014) analysis is based on only three events, all discovered by amateur astronomers over a span of three decades. It is impossible to accurately quantify the completeness associated with the discoveries in this sample. It is thus possible that the LRN luminosity function at low luminosities differs from that derived by Kochanek et al. (2014). For example, as discussed in their paper, if they assume that the searches that discovered the Galactic LRNe had a shallower limiting magnitude (m lim, I = 9 mag instead of 13), their luminosity function scales as $L^{-1.7\pm0.5}$. This is closer to the value derived in this paper for the more-luminous extragalactic LRNe. A systematic census of Galactic stellar mergers is required to confirm the slope of the luminosity function at low luminosities.

The broken power-law shape, if confirmed, has interesting implications for our sample of LRNe. Observations as well as theoretical models of LRNe predict that the peak luminosities and durations of LRNe directly correlate with their progenitor masses (Ivanova et al. 2013a; Kochanek et al. 2014; Blagorodnova et al. 2021; Cai et al. 2022; Matsumoto & Metzger 2022). Using the relation $L \propto M^{-2.2\pm0.3}$ from Cai et al. (2022), our luminosity scaling implies a mass function of $dN/dM \propto M^{-4.3\pm1.1}$, different from standard IMF models. Kochanek et al. (2014) found that the lower-luminosity Galactic LRNe have progenitors consistent with the stellar IMF. An interesting possibility to explain this difference is to postulate that the low-luminosity Galactic events are mergers while the more luminous extragalactic events are CE ejections. For a binary system with a given primary mass, the associated LRN is brighter and longer-lived if it undergoes complete CE ejection rather than a merger where only a small fraction of the envelope is ejected. From their simulations, Howitt et al. (2020) find that the bright LRNe ($M_{\rm bol} \leqslant -10$ mag) result almost exclusively from envelope ejections, while mergers result in lower-luminosity transients. The broken power law would then suggest that the luminous CE ejections are much rarer than the less luminous stellar mergers. The range of peak luminosities and durations of the ZTF sample events presented here is consistent with the CE ejections of Howitt et al. (2020). Thus, in this picture, most if not all of the events in the ZTF sample analyzed here could be CE ejections. In this case, our derived rate would represent the rate of CE ejections in massive binaries—an important step in the formation of double compact objects (DCOs; Vigna-Gómez et al. 2020).

It is interesting to compare our rate to the rate of DCO mergers detected by LIGO. The LIGO Scientific Collaboration, the Virgo Collaboration, the KAGRA Collaboration, et al. (2021b) determined the volumetric rates of binary neutron star (BNS), neutron star–black hole (NSBH), and binary black hole (BBH) mergers to be 10–1700 $\rm Gpc^{-3}\,yr^{-1}$, 7.8–140 $\rm Gpc^{-3}\,yr^{-1}$, and 17–44 $\rm Gpc^{-3}\,yr^{-1}$, respectively. The shaded pink regions in Figure 12 indicate these DCO merger rates. The plot shows that the brightest LRNe are consistent with a significant fraction of them being progenitors of DCO mergers. However, we reiterate that there is no direct evidence to suggest that the more luminous LRNe come from CE ejections as opposed to mergers. Klencki et al. (2021) show that, for successful CE in DCO progenitors, the primary needs to be a convective-envelope red supergiant (RSG), contrary to the few LRNe with progenitor identifications where the progenitor is a yellow supergiant with a radiative envelope. While none of the very luminous ($M_{\rm r} \leqslant -15$ mag) LRNe have progenitor identifications, it remains to be seen whether their photometric and spectroscopic properties conform to those expected from an RSG-CE ejection.

Finally, we note another possible source of bias that could affect the LRN rate determined here. Metzger & Pejcha (2017) predict a population of LRNe originating in mergers involving giant primaries that should be completely enshrouded by dust and emit most of their radiation at IR wavelengths. MacLeod et al. (2022) also show that dust formation in pre-merger outflows could obscure the binary system, causing the resulting LRNe to be observable only at IR wavelengths. Some of the IR-only transients (dubbed SPRITES) that were discovered by the Spitzer Space Telescope and had no optical counterparts are potential examples of such dust-enshrouded LRNe (Kasliwal et al. 2017). Searches for LRNe at IR wavelengths are required to probe this dust-enshrouded population of LRNe. Upcoming NIR time-domain surveys such as the Wide-field Infrared Transient Explorer (WINTER; Lourie et al. 2020) at Palomar Observatory and Dynamic REd All-sky Monitoring Survey (DREAMS; Soon et al. 2020) at Siding Springs Observatory that are slated to commence operations in the first half of 2023 will help achieve this. Targeted surveys of nearby galaxies with these NIR telescopes will help discover and study IR-only LRNe, as well as shed light on the complete LRN landscape. Additionally, as all LRNe are brighter and longer-lived at NIR wavelengths than in the optical, the NIR surveys will also increase the population of optically selected LRNe similar to those presented in this paper. Of particular importance will be additional discoveries of lower-luminosity LRNe ($-9.5 > M_{r,\rm peak} > -11$ mag)—a luminosity range that has not been probed by our sample, as they have much shorter optical light curves and can lack the early blue optical peak seen in their brighter counterparts (Blagorodnova et al. 2021). The upcoming NIR surveys will thus provide an unbiased and more precise measurement of the LRN luminosity function and volumetric rate.

4.2. ILRTs

We derive an ILRT rate of $R_{<-13.5} \approx 2.6 \times 10^{-6}$ $\rm Mpc^{-3}\,yr^{-1}$ for ILRTs that are more luminous than $M_r = -13.5$ mag. This rate is smaller than the LRN rate by two orders of magnitude, but we note that the luminosity threshold of our ILRT sample is brighter than that of our LRN sample. We cannot constrain the luminosity function of ILRTs with luminosities lower than $M_r = -13.5$ mag, as none of our events lie in this luminosity range. In the literature, there are four ILRTs with $-12 \geqslant M_r \geqslant -13.5$ mag, all discovered long before the start of ZTF (Cai et al. 2021). Assuming our luminosity function extends to $M_r \approx -12$ mag, the total rate of ILRTs is $R_{<-12} \approx 2 \times 10^{-5}$ $\rm Mpc^{-3}\,yr^{-1}$. Additional discoveries of ILRTs in this low-luminosity range are required in order to map out the lower end of the ILRT luminosity function.

Cai et al. (2021) derived a lower limit on the ILRT rate of 9×10^{-6} $\rm Mpc^{-3}\,yr^{-1}$. They used a sample of 12 ILRTs discovered in the last 12 yr within 30 Mpc to estimate the ILRT rate, but their analysis did not include a luminosity function or completeness of the surveys. Additionally, their sample included two events with lower luminosities than our threshold, and their lower limit is consistent with the rough estimate $R_{<-12}$ above. Comparing to the core-collapse SN rate of $\sim 1.01 \times 10^{-4}$ $\rm Mpc^{-3}\,yr^{-1}$ (Perley et al. 2020), we find that the rate of ILRTs ($R_{<-13.5}$) is $\sim 3^{+1.5}_{-1.5}\%$ of the CCSN rate. It remains to be seen how much the lower-luminosity events contribute to this rate.

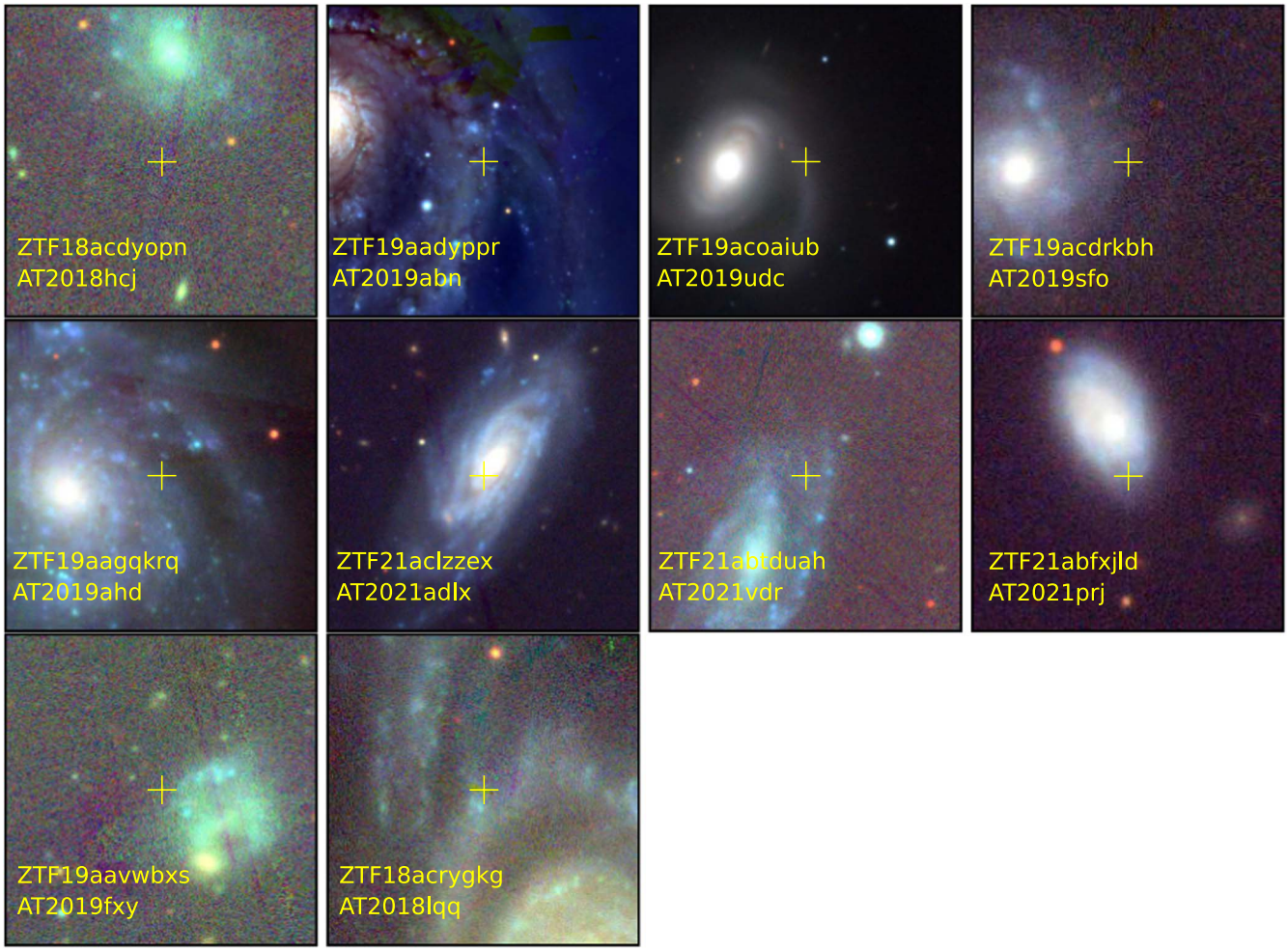

Figure 13. Host galaxies of the ILRTs in our sample. The positions of the ILRTs are indicated with a yellow cross, on top of color-coded PS1 images obtained from http://ps1images.stsci.edu/cgi-bin/ps1cutouts. Similarly to LRNe, all ILRTs in our sample are located in star-forming galaxies.

Our rate is also lower than that of Thompson et al. (2009), who estimated the ILRT rate is ∼20% of the CCSN rate based on the two ILRTs SN 2008S and NGC 300OT. We note that NGC 300OT is below the luminosity threshold of our sample, and the rough estimate $R_{<-12}$ is consistent with their result.

Given the possible association of ILRT with ECSNe, it is worth comparing our rate to theoretical predictions. Poelarends et al. (2008) determine the range of stellar masses expected to undergo ECSN for different mass-loss and convective dredge-up prescriptions, and they determine their rate to be ∼4%–24% of the CCSN rate. The rate also depends sensitively on the metallicity; for example, Poelarends (2007) find that, for $Z = 0.02$, the ECSN rate is ∼3% of the CCSN rate, but for $Z = 10^{-4}$, the rate is ∼25%. On the other hand, Doherty et al. (2015) use a different metallicity dependence for the mass-loss rate and find that the ECSN rate is ∼2%–5% of the CCSN rate for all metallicities in the range $Z = [10^{-5}, 0.02]$. Our measured ILRT rate ($R_{<-13.5}$) is on the lower side, but still consistent with the wide range of theoretical calculations, and it is in line with the interpretation that several ILRTs could be ECSNe.

However, we cannot rule out the possibility that some of the ILRTs presented here are LBV outbursts. Dusty LBV outbursts can also result in red, low-luminosity transients with spectra showing narrow H with Ca II and [Ca II] features, similarly to ILRTs (Andrews et al. 2021). While the transients in our sample do not show any archival activity for the last ∼10 yr, it is possible that they experienced previous outbursts. Nevertheless, the connection of IRLTs to ECSNe is supported by strong evidence related to their dust-enshrouded progenitors with masses of 8–15 $M_{\odot}$ (Botticella et al. 2009; Thompson et al. 2009; Jencson et al. 2019) and the fact that their remnants faded below their progenitor luminosities (Adams et al. 2016). Progenitors are not detectable for most of the ILRTs in our sample. As this will also be the case for a large number of ILRTs that will be detected by future large-scale deep surveys such as the Vera Rubin Observatory (VRO; Ivezić et al. 2019), it is important to identify additional ways of distinguishing ILRTs from LBV outbursts in order to confirm their nature as ECSNe. Possible ways to achieve this include extensive nebular-phase observations of ILRTs. On the one hand, late-time photometric observations would allow us to detect the presence and estimate the amount of Ni generated in the explosion (see Cai et al. 2021). On the other hand, nebular spectroscopic observations would allow us to determine the composition of the ILRT ejecta where the presence of stronger Ni than Fe lines, weak O, Mg, C, and Fe lines, and a low [O I]/[Ca II] ratio would be evidence for the ECSN scenario (similar to AT 2018zd; Hiramatsu et al. 2021).

4.3. Host Galaxies of LRNe and ILRTs

Figure 13 shows thumbnails of the host galaxies of the ZTF ILRTs presented in this paper. The ZTF ILRTs belong to star-

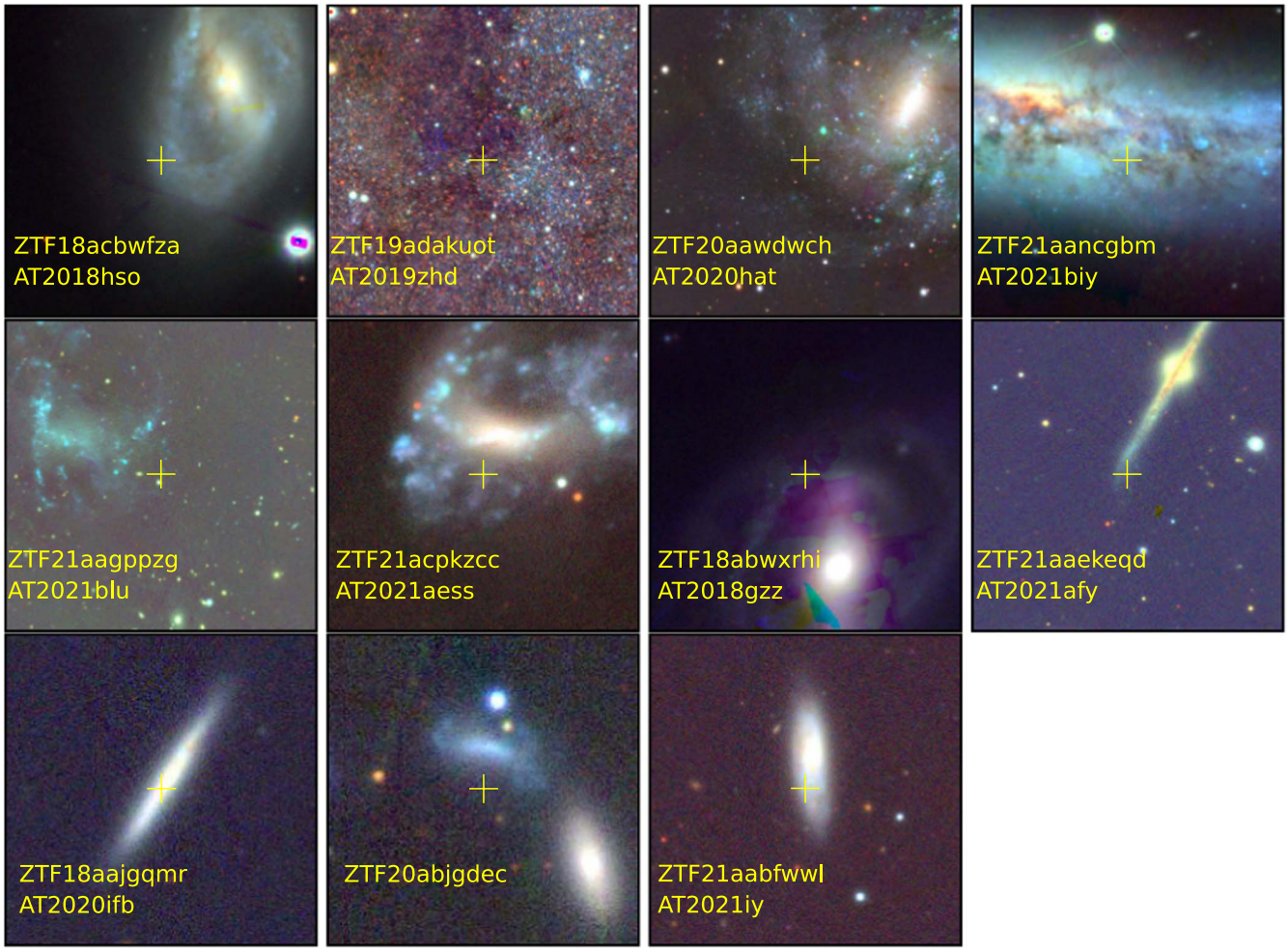

Figure 14. Host galaxies of the LRNe in our sample. The positions of the LRNe are indicated with a yellow cross. ZTF 19adakuot is located in M31. All LRNe in our sample (including LRN-bronze events) are located in star-forming galaxies.

forming galaxies, similarly to all ILRTs discovered to date (see Cai et al. 2021). As neither ZTF nor the CLU galaxy catalog are biased toward star-forming galaxies (Cook et al. 2019), the sample confirms that ILRTs occur in predominantly young environments—consistent with their ECSN or LBV interpretations.

Figure 14 shows thumbnails of the host galaxies of the ZTF LRNe presented in this paper. All ZTF LRNe also belong to late-type star-forming galaxies (see Table 1 for host-galaxy morphologies), similarly to all LRNe discovered in the last decade (see Pastorello et al. 2019a; Blagorodnova et al. 2021). This confirms that the luminous ($M_r \leqslant -11$ mag) LRNe occur more commonly in star-forming environments. This is consistent with the expectation that LRNe in this luminosity range have massive ($\geqslant 10\,M_\odot$) progenitors (Blagorodnova et al. 2021). Early-type galaxies are expected to have LRNe with lower-mass progenitors and hence lower luminosities, making time-domain surveys less sensitive to detecting them.

Only three LRNe have been discovered in old environments: OGLE 2002-BLG-360 in the Galactic bulge (Tylenda et al. 2013), M31RV in the bulge of M31 (Rich et al. 1989), and M85 OT in the S0-type galaxy M85 (Kulkarni et al. 2007). Of these, M85 OT does not follow the LRN peak luminosity versus progenitor mass correlation (Kochanek et al. 2014; Blagorodnova et al. 2021). The progenitor mass of M85 OT has been constrained to $<7\,M_\odot$ (Ofek et al. 2008). This is expected to produce an LRN with $M_{r,\mathrm{peak}} \geqslant -10$ mag—much fainter than its actual peak $M_r \approx -12$ mag. As it is not a canonical LRN, M85 OT has been suggested to be an ILRT. However, ILRTs have star-forming hosts, unlike M85 OT. Its progenitor mass is also incompatible with the ECSN or LBV scenario for ILRTs, suggesting that it is not a canonical ILRT either. An intriguing possibility is that M85 OT is the merger of a white dwarf (WD) with a companion evolved star. Such "CV mergers" are believed to produce transients with observational characteristics similar to those of LRNe (Metzger et al. 2021). A WD progenitor would be consistent with the old environment of M85 OT. As this is not a canonical merger of two stars, we would not expect the transient to follow the correlations observed in other LRNe. The Galactic slow nova CK Vul has been proposed to be a merger involving a WD progenitor (Eyres et al. 2018; Metzger et al. 2021). M85 OT could be an extragalactic member of this class of outbursts. Discoveries of additional LRNe in early-type galaxies will shed further light on the origin of this population.

5. Summary and the Future

Despite the discovery of a dozen LRNe and ILRTs in the last decade, their rate remained uncertain. In this paper, we compiled a systematic sample of LRNe and ILRTs using the Census of the Local Universe experiment on the Zwicky

Transient Facility to address this issue. We present a sample of eight LRNe and eight ILRTs identified by the CLU experiment. We discuss the properties of these transients and present new data for the precursor emission in AT 2019zhd and line-profile evolution in ZTF 21aaekeqd (AT 2021afy). We conduct simulations of the ZTF survey using actual ZTF observation history and correct for the completeness of CLU to derive a rate of $7.8^{+6.5}_{-3.7} \times 10^{-5}$ Mpc^{-3} yr^{-1} for LRNe with absolute magnitudes M_r in the range $[-11, -16]$, and $2.6^{+1.8}_{-1.4} \times 10^{-6}$ Mpc^{-3} yr^{-1} for ILRTs with $M_r < -13.5$ mag.

The rates of LRNe in this luminosity range are much lower than those extrapolated from Galactic measurements of low-luminosity Galactic LRNe by Kochanek et al. (2014). Specifically, we find that the luminosity function of LRNe scales as $\propto L^{-2.5}$ in the range $-11 > M_r > -16$ mag, as opposed to $L^{-1.4}$ derived by Kochanek et al. (2014) for $-4\,M_V > -10$ mag. This steeper decline at higher luminosities is broadly consistent with binary population synthesis models of Howitt et al. (2020); however, the BPS models underpredict the rates for $M_r < -13$ mag by as much as two orders of magnitude. This discrepancy is likely due to assumptions about the light-curve models used in the BPS simulation. The rates of the brightest LRNe in our sample are consistent with a significant fraction of them being progenitors of double compact object systems. We note that all LRNe in our sample and those discovered in the last decade belong to star-forming host galaxies. There have been no analogs of M85 OT, which was discovered in an S0-type galaxy.

The ILRT rate corresponds to $2.6^{+1.8}_{-1.4}$% of the local core-collapse SN rate. However, our sample only probes the high-luminosity end of the ILRT luminosity function. Assuming our scaling extrapolates to lower luminosities, our measurement is consistent with previously measured constraints on the ILRT rate by Thompson et al. (2009) and Cai et al. (2021). The ILRT rate is also consistent with the wide range of theoretical predictions of rates of electron-capture SNe by Poelarends et al. (2008) and Doherty et al. (2015). Additional nebular-phase observations of ILRTs and observations of their progenitors are required in order to confidently establish them as electron-capture SNe.

The future holds exciting prospects for studies of LRNe and ILRTs. Upcoming NIR time-domain surveys such as WINTER and DREAMS will enable substantial progress in the next few years. These surveys will provide the first unbiased sample of the dusty, red transients and will be instrumental in uncovering hidden populations that could be missed by optical surveys. These results will set the stage for the Vera Rubin Observatory. Based on our rate estimates, we calculate that VRO will discover between 300–1500 LRNe and 200–700 ILRTs (with $M_{r,\mathrm{peak}} < -13.5$ mag) per year (assuming a sensitivity of $m_r \approx 24.2$ mag). While most of these will be too faint for spectroscopic classifications, these transients can be identified based on their low luminosities, long-duration light curves, and red photometric colors. An experiment similar to CLU that keeps track of VRO transients in cataloged galaxies will be instrumental in the study of LRNe and ILRTs.

We thank the anonymous referee for providing useful comments. This work is based on observations obtained with the Samuel Oschin 48 inch Telescope and the 60 inch Telescope at Palomar Observatory as part of the Zwicky Transient Facility (ZTF) project. ZTF is supported by the National Science Foundation (NSF) under grants AST-1440341 and AST-2034437, and a collaboration including current partners Caltech, IPAC, the Weizmann Institute of Science, the Oskar Klein Center at Stockholm University, the University of Maryland, Deutsches Elektronen-Synchrotron and Humboldt University, the TANGO Consortium of Taiwan, the University of Wisconsin at Milwaukee, Trinity College Dublin, Lawrence Livermore National Laboratories, IN2P3, University of Warwick, Ruhr University Bochum, Northwestern University, and former partners the University of Washington, Los Alamos National Laboratories, and Lawrence Berkeley National Laboratories. Operations are conducted by COO, IPAC, and UW. The ZTF forced-photometry service was funded under the Heising-Simons Foundation grant 12540303 (PI M. Graham). The SED Machine is based upon work supported by the NSF under grant 1106171.

This work is also based in part on observations made with the Nordic Optical Telescope, owned in collaboration by the University of Turku and Aarhus University, and operated jointly by Aarhus University, the University of Turku, and the University of Oslo (respectively representing Denmark, Finland, and Norway), the University of Iceland, and Stockholm University, at the Observatorio del Roque de los Muchachos, La Palma, Spain, of the Instituto de Astrofísica de Canarias. The Liverpool Telescope is operated on the island of La Palma by Liverpool John Moores University in the Spanish Observatorio del Roque de los Muchachos of the Instituto de Astrofísica de Canarias with financial support from the UK Science and Technology Facilities Council. This work is part of the research program VENI, with project No. 016.192.277, which is partially financed by the Netherlands Organisation for Scientific Research (NWO).

A major upgrade of the Kast spectrograph on the Shane 3 m telescope at Lick Observatory, led by Brad Holden, was made possible through generous gifts from the Heising-Simons Foundation, William and Marina Kast, and the University of California Observatories. Research at Lick Observatory is partially supported by a generous gift from Google. Some of the data presented herein were obtained at the W. M. Keck Observatory, which is operated as a scientific partnership among the California Institute of Technology, the University of California, and NASA; the observatory was made possible by the generous financial support of the W. M. Keck Foundation. A.V.F.'s group acknowledges generous support from the Christopher R. Redlich Fund, Sunil Nagaraj, Landon Noll, Sandy Otellini, and many additional donors.

Data Availability

Light curves and spectra of the LRNe, ILRTs, and possible LBVs presented in this paper, as well as template LRN and ILRT light curves, will be made available online after publication at Zenodo (DOI:10.5281/zenodo.7651607). The spectra will also be posted to WISeREP. The ZTF pointing-history logs will be made available upon request to the corresponding author.

Appendix
Properties of Sources Classified as Possible LBV Outbursts

The light curves of the six sources we classify as potential LBV outbursts are shown in Figure 15, and their spectra are displayed in Figure 16. We discuss the individual objects below.

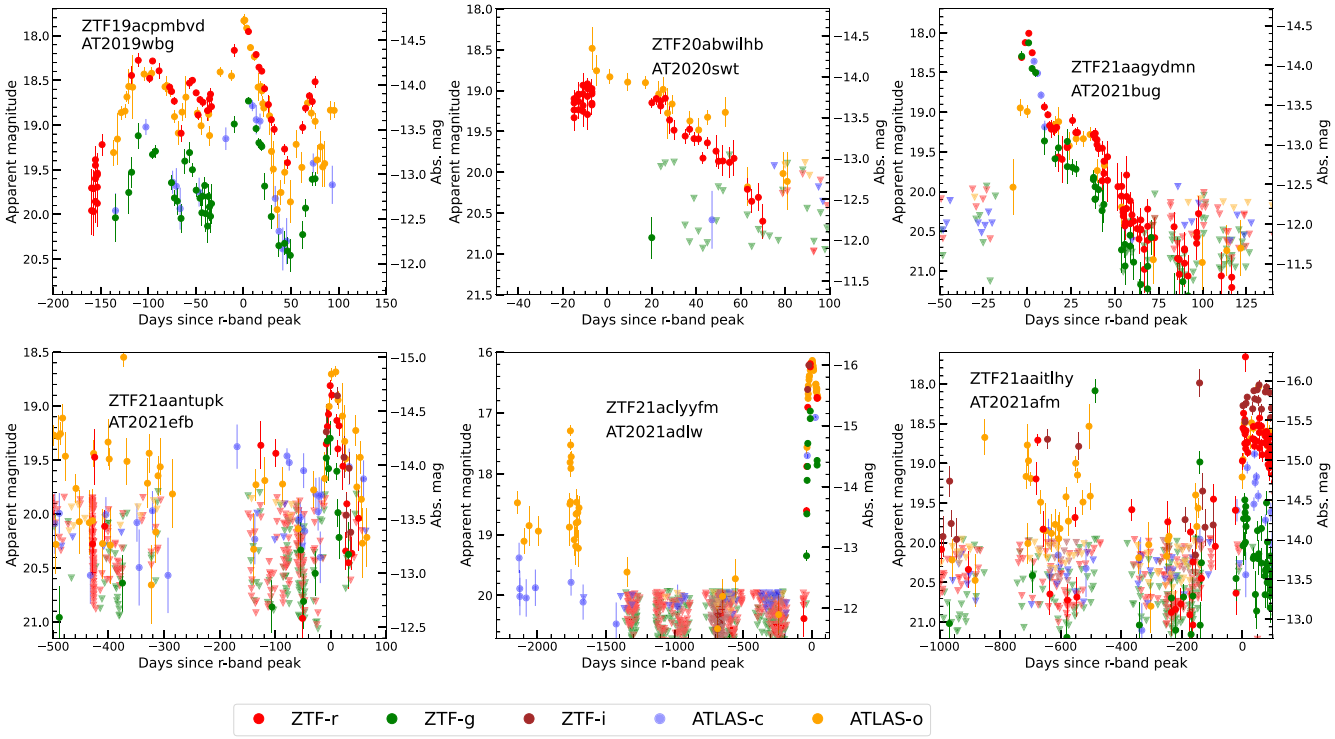

Figure 15. Light curves of transients that are possible LBV outbursts.

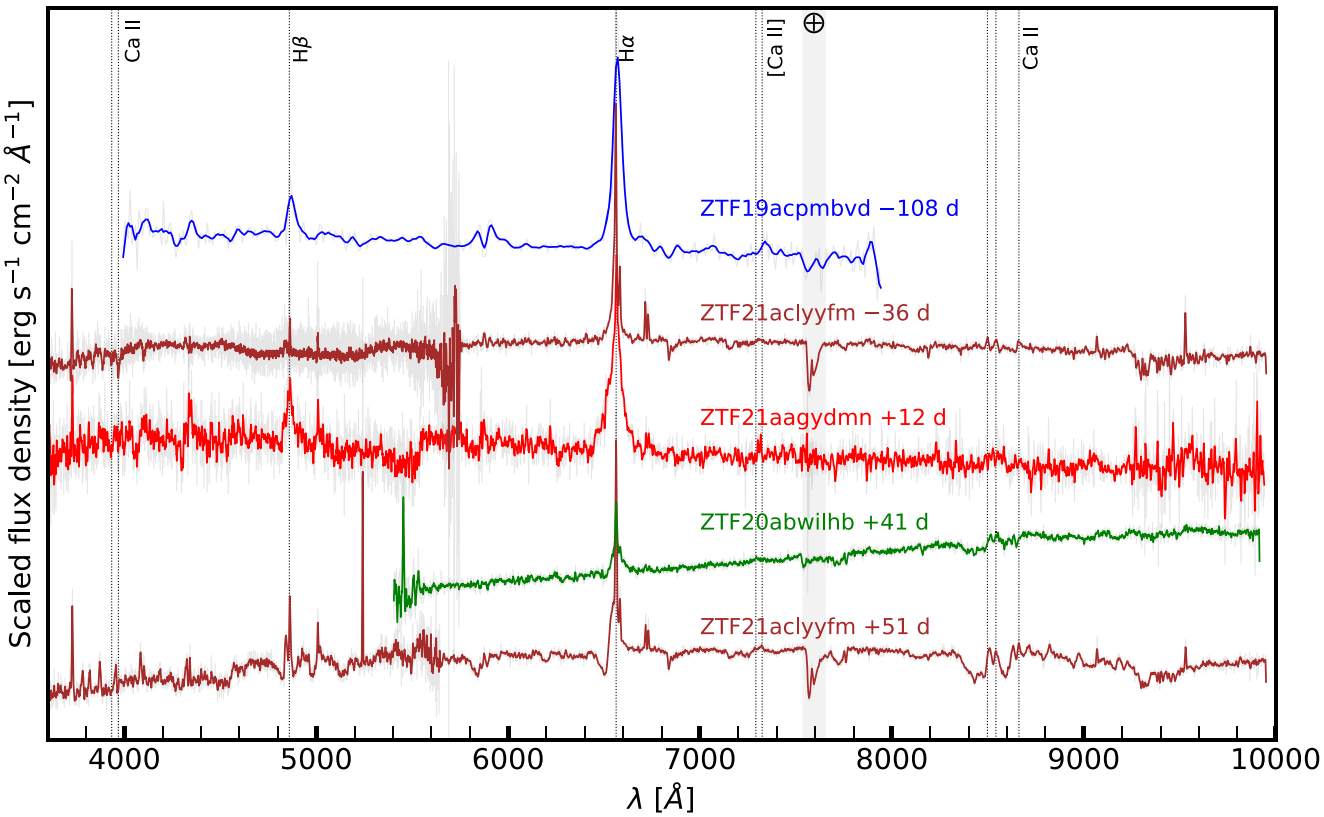

Figure 16. Optical spectra of transients that are possible LBV outbursts.

1. ZTF 19acpmbvd (AT 2019wbg) is located in the galaxy NGC 4045 and shows a bumpy, red light curve with at least three peaks. The transient was detected in 2016 in iPTF data with $m_g \approx 22$ mag. It was redetected in ZTF in 2022 at $m_r \approx 19.5$ mag. A spectrum taken during this outburst shows Hα emission with $v_{\rm FWHM} \approx 1700$ km s^{-1}.
2. ZTF 20abwilhb (AT 2020swt) is located in the galaxy UGC 03820. The light curve does not show multiple

peaks, but it exhibits signs of a ∼40 day plateau, after which the transient declines. The optical spectrum has Hα emission with $v_{\rm FWHM} \approx 3300$ km s^{-1}, suggesting that this transient could be an LBV outburst or a low-luminosity Type II SN.

3. ZTF 21aagydmn (AT 2021bug) is located in the galaxy NGC 4533 and exhibits an unusual light curve that peaks at $M_r \approx -14.4$ mag, thereafter declining quickly. Once off the first decline, the light curve plateaus for ∼10 days and then continues to decline. The spectrum shows Hα emission with $v_{\rm FWHM} \approx 2600$ km s^{-1}; however, the light curve does not have a long-duration plateau as seen in low-luminosity Type II SNe. The true nature of this source is unclear, but an outburst in a massive star is a possibility.
4. ZTF 21aantupk (AT 2021efb) is located at the nucleus of the galaxy CGC 003-005. The light curve shows erratic activity in the ATLAS and the ZTF data for several hundred days prior to the main explosion in 2021. We suggest that this source is either an LBV outburst or AGN activity.
5. ZTF 21aclyyfm (AT 2021adlw) is located in the galaxy NGC 3813, and it reached $M_r \approx -16$ mag in the 2021 outburst. Archival ATLAS data show that it underwent a similar outburst ($M_o \approx -15$ mag) about 1800 days prior to this outburst. An optical spectrum taken at an early phase during the 2021 outburst shows narrow Hα emission with $v_{\rm FWHM} \approx 1000$ km s^{-1}; however, late-time spectra reveal ejecta with much larger velocities. This source is likely an LBV outburst or a "weak" Type IIn SN.
6. ZTF 21aaitlhy (AT 2021afm) is located close to the center of the galaxy NGC 5657. It had several detections in ATLAS and ZTF data in the ∼1000 days leading up to the 2021 explosion. We also detect the transient in the g band in PTF data taken during 2011 July and 2016 April at $m_g \approx 20$ mag. Owing to the extensive archival activity, we categorize this source as a possible LBV outburst.

ORCID iDs

Viraj R. Karambelkar https://orcid.org/0000-0003-2758-159X
Mansi M. Kasliwal https://orcid.org/0000-0002-5619-4938
Nadejda Blagorodnova https://orcid.org/0000-0003-0901-1606
Jesper Sollerman https://orcid.org/0000-0003-1546-6615
Robert Aloisi https://orcid.org/0000-0003-2822-616X
Shreya G. Anand https://orcid.org/0000-0003-3768-7515
Igor Andreoni https://orcid.org/0000-0002-8977-1498
Thomas G. Brink https://orcid.org/0000-0001-5955-2502
Rachel Bruch https://orcid.org/0000-0001-8208-2473
David Cook https://orcid.org/0000-0002-6877-7655
Kaustav Kashyap Das https://orcid.org/0000-0001-8372-997X
Andrew Drake https://orcid.org/0000-0003-0228-6594
Alexei V. Filippenko https://orcid.org/0000-0003-3460-0103
Christoffer Fremling https://orcid.org/0000-0002-4223-103X
Anna Ho https://orcid.org/0000-0002-9017-3567
Jacob Jencson https://orcid.org/0000-0001-5754-4007
David Jones https://orcid.org/0000-0003-3947-5946
Russ R. Laher https://orcid.org/0000-0003-2451-5482
Frank J. Masci https://orcid.org/0000-0002-8532-9395
Kishore C. Patra https://orcid.org/0000-0002-1092-6806
Josiah Purdum https://orcid.org/0000-0003-1227-3738
Tawny Sit https://orcid.org/0000-0001-8208-9755
Yashvi Sharma https://orcid.org/0000-0003-4531-1745
Anastasios Tzanidakis https://orcid.org/0000-0003-0484-3331
Stéfan J. van der Walt https://orcid.org/0000-0001-9276-1891
Yuhan Yao https://orcid.org/0000-0001-6747-8509
Chaoran Zhang https://orcid.org/0000-0002-0331-6727

References

Adams, S. M., Kochanek, C. S., Prieto, J. L., et al. 2016, MNRAS, 460, 1645
Andrews, J. E., Jencson, J. E., Van Dyk, S. D., et al. 2021, ApJ, 917, 63
Bellm, E. C., Kulkarni, S. R., Graham, M. J., et al. 2019, PASP, 131, 018002
Bildsten, L., Shen, K. J., Weinberg, N. N., & Nelemans, G. 2007, ApJL, 662, L95
Blagorodnova, N., Karambelkar, V., Adams, S. M., et al. 2020, MNRAS, 496, 5503
Blagorodnova, N., Klencki, J., Pejcha, O., et al. 2021, A&A, 653, A134
Blagorodnova, N., Neill, J. D., Walters, R., et al. 2018, PASP, 130, 035003
Botticella, M. T., Pastorello, A., Smartt, S. J., et al. 2009, MNRAS, 398, 1041
Bramall, D. G., Sharples, R., Tyas, L., et al. 2010, Proc. SPIE, 7735, 77354F
Cai, Y. Z., Pastorello, A., Fraser, M., et al. 2019, A&A, 632, L6
Cai, Y. Z., Pastorello, A., Fraser, M., et al. 2021, A&A, 654, A157
Cai, Y. Z., Pastorello, A., Fraser, M., et al. 2022, arXiv:2207.00734
Cook, D. O., Kasliwal, M. M., Van Sistine, A., et al. 2019, ApJ, 880, 7
Davis, K., Jones, D., Bustamante-Rosell, M. J., Siebert, M., & Foley, R. 2021, TNSCR, 3967, 1
De, K., Kasliwal, M. M., Tzanidakis, A., et al. 2020, ApJ, 905, 58
Dekany, R., Smith, R. M., Riddle, R., et al. 2020, PASP, 132, 038001
Doherty, C. L., Gil-Pons, P., Siess, L., Lattanzio, J. C., & Lau, H. H. B. 2015, MNRAS, 446, 2599
Eyres, S. P. S., Evans, A., Zijlstra, A., et al. 2018, MNRAS, 481, 4931
Feindt, U., Nordin, J., Rigault, M., et al. 2019, JCAP, 2019, 005
Fremling, C., Miller, A. A., Sharma, Y., et al. 2020, ApJ, 895, 32
Graham, M. J., Kulkarni, S. R., Bellm, E. C., et al. 2019, PASP, 131, 078001
Herter, T. L., Henderson, C. P., Wilson, J. C., et al. 2008, Proc. SPIE, 7014, 70140X
Hinkle, J. 2021, TNSCR, 64, 1
Hiramatsu, D., Howell, D. A., Van Dyk, S. D., et al. 2021, NatAs, 5, 903
Howitt, G., Stevenson, S., Vigna-Gómez, A., et al. 2020, MNRAS, 492, 3229
Humphreys, R. M., Bond, H. E., Bedin, L. R., et al. 2011, ApJ, 743, 118
Humphreys, R. M., Davidson, K., & Smith, N. 1999, PASP, 111, 1124
Ivanova, N., Justham, S., Avendano Nandez, J. L., & Lombardi, J. C. 2013a, Sci, 339, 433
Ivanova, N., Justham, S., Chen, X., et al. 2013b, A&ARv, 21, 59
Jencson, J. E., Adams, S. M., Bond, H. E., et al. 2019, ApJL, 880, L20
Ivezić, Ž., Kahn, S. M., Tyson, J. A., et al. 2019, ApJ, 873, 111
Kamiński, T., Mason, E., Tylenda, R., & Schmidt, M. R. 2015, A&A, 580, A34
Kamiński, T., & Tylenda, R. 2011, A&A, 527, A75
Karambelkar, V. R., Kasliwal, M. M., Maguire, K., et al. 2021, ApJL, 921, L6
Kasliwal, M. M., Bally, J., Masci, F., et al. 2017, ApJ, 839, 88
Kasliwal, M. M., Kulkarni, S. R., Arcavi, I., et al. 2011, ApJ, 730, 134
Kim, Y. L., Rigault, M., Neill, J. D., et al. 2022, PASP, 134, 024505
Klencki, J., Nelemans, G., Istrate, A. G., & Chruslinska, M. 2021, A&A, 645, A54
Kochanek, C. S., Adams, S. M., & Belczynski, K. 2014, MNRAS, 443, 1319
Kulkarni, S. R., Ofek, E. O., Rau, A., et al. 2007, Natur, 447, 458
Law, N. M., Kulkarni, S. R., Dekany, R. G., et al. 2009, PASP, 121, 1395
Licquia, T. C., & Newman, J. A. 2015, ApJ, 806, 96
Lourie, N. P., Baker, J. W., Burruss, R. S., et al. 2020, Proc. SPIE, 11447, 114479K
MacLeod, M., De, K., & Loeb, A. 2022, arXiv:2205.07929
MacLeod, M., Macias, P., Ramirez-Ruiz, E., et al. 2017, ApJ, 835, 282
Madau, P., & Dickinson, M. 2014, ARA&A, 52, 415
Masci, F. J., Laher, R. R., Rusholme, B., et al. 2019, PASP, 131, 018003
Matsumoto, T., & Metzger, B. D. 2022, arXiv:2202.10478
Metzger, B. D., & Pejcha, O. 2017, MNRAS, 471, 3200

Metzger, B. D., Zenati, Y., Chomiuk, L., Shen, K. J., & Strader, J. 2021, ApJ, 923, 100
Moe, M., & Di Stefano, R. 2017, ApJS, 230, 15
Munari, U., Henden, A., Kiyota, S., et al. 2002, A&A, 389, L51
Ofek, E. O., Kulkarni, S. R., Rau, A., et al. 2008, ApJ, 674, 447
Oke, J. B., Cohen, J. G., Carr, M., et al. 1995, PASP, 107, 375
Oke, J. B., & Gunn, J. E. 1982, PASP, 94, 586
Pastorello, A., Chen, T.-W., Cai, Y.-Z., et al. 2019b, A&A, 625, L8
Pastorello, A., & Fraser, M. 2019, NatAs, 3, 676
Pastorello, A., Fraser, M., Valerin, G., et al. 2021a, A&A, 646, A119
Pastorello, A., Mason, E., Taubenberger, S., et al. 2019a, A&A, 630, A75
Pastorello, A., Valerin, G., Fraser, M., et al. 2021b, A&A, 647, A93
Pastorello, A., Valerin, G., Fraser, M., et al. 2022, arXiv:2208.02782
Pejcha, O., Metzger, B. D., Tyles, J. G., & Tomida, K. 2017, ApJ, 850, 59
Perley, D. A., Fremling, C., Sollerman, J., et al. 2020, ApJ, 904, 35
Poelarends, A. J. T. 2007, PhD thesis, Univ. Utrecht, Netherlands
Poelarends, A. J. T., Herwig, F., Langer, N., & Heger, A. 2008, ApJ, 675, 614
Politano, M., van der Sluys, M., Taam, R. E., & Willems, B. 2010, ApJ, 720, 1752
Poznanski, D., Prochaska, J. X., & Bloom, J. S. 2012, MNRAS, 426, 1465
Prieto, J. L., Kistler, M. D., Thompson, T. A., et al. 2008, ApJL, 681, L9
Rau, A., Kulkarni, S. R., Law, N. M., et al. 2009, PASP, 121, 1334
Reguitti, A., Pumo, M. L., Mazzali, P. A., et al. 2021, MNRAS, 501, 1059
Rich, R. M., Mould, J., Picard, A., Frogel, J. A., & Davies, R. 1989, ApJL, 341, L51
Rigault, M., Neill, J. D., Blagorodnova, N., et al. 2019, A&A, 627, A115
Schlafly, E. F., & Finkbeiner, D. P. 2011, ApJ, 737, 103
Schlafly, E. F., Finkbeiner, D. P., Jurić, M., et al. 2012, ApJ, 756, 158
Smith, K. W., Shingles, L., Srivastav, S., et al. 2021a, TNSAN, 33, 1
Smith, K. W., Smartt, S. J., Young, D. R., et al. 2020, PASP, 132, 085002
Smith, K. W., Srivastav, S., McBrien, O., et al. 2021b, TNSAN, 43, 1
Smith, N., Andrews, J. E., Mauerhan, J. C., et al. 2016, MNRAS, 455, 3546
Smith, N., Ganeshalingam, M., Chornock, R., et al. 2009, ApJL, 697, L49
Smith, N., Li, W., Silverman, J. M., Ganeshalingam, M., & Filippenko, A. V. 2011, MNRAS, 415, 773
Soker, N. 2020, ApJ, 893, 20
Soker, N., & Kaplan, N. 2021, RAA, 21, 090
Soon, J., Adams, D., De, K., et al. 2020, Proc. SPIE, 11203, 1120307
The LIGO Scientific Collaboration, the Virgo Collaboration, the KAGRA Collaboration, et al. 2021a, arXiv:2111.03606
The LIGO Scientific Collaboration, the Virgo Collaboration, the KAGRA Collaboration, et al. 2021b, arXiv:2111.03634
Thompson, T. A., Prieto, J. L., Stanek, K. Z., et al. 2009, ApJ, 705, 1364
Tonry, J. L., Denneau, L., Heinze, A. N., et al. 2018, PASP, 130, 064505
Tsuna, D., Ishii, A., Kuriyama, N., Kashiyama, K., & Shigeyama, T. 2020, ApJL, 897, L44
Turatto, M., Benetti, S., & Cappellaro, E. 2003, in From Twilight to Highlight: The Physics of Supernovae, ed. W. Hillebrandt & B. Leibundgut (Berlin: Springer), 200
Tylenda, R. 2005, A&A, 436, 1009
Tylenda, R., Hajduk, M., Kamiński, T., et al. 2011, A&A, 528, A114
Tylenda, R., Kamiński, T., Udalski, A., et al. 2013, A&A, 555, A16
Uno, K., Kawabata, M., & Taguchi, K. 2021, TNSCR, 393, 1
van der Walt, S. J., Crellin-Quick, A., & Bloom, J. S. 2019, JOSS, 4, 1247
Vigna-Gómez, A., MacLeod, M., Neijssel, C. J., et al. 2020, PASA, 37, e038
Wilson, J. C., Henderson, C. P., Herter, T. L., et al. 2004, Proc. SPIE, 5492, 1295
Yang, S., Sollerman, J., Strotjohann, N. L., et al. 2021, A&A, 655, A90